The Role of Upper-Level Coupling on Great Plains Low-Level Jet Structure and Variability

D. ALEX BURROWS,[a,b] CRAIG R. FERGUSON,[a,b] AND LANCE F. BOSART[b]

[a] *Atmospheric Sciences Research Center, University at Albany, State University of New York, Albany, New York;* [b] *Department of Atmospheric and Environmental Sciences, University at Albany, State University of New York, Albany, New York*

(Manuscript received 28 February 2020, in final form 31 July 2020)

ABSTRACT: The Great Plains (GP) southerly nocturnal low-level jet (GPLLJ) is a dominant contributor to the region's warm-season (May–September) mean and extreme precipitation, wind energy generation, and severe weather outbreaks—including mesoscale convective systems. The spatiotemporal structure, variability, and impact of individual GPLLJ events are closely related to their degree of upper-level synoptic coupling, which varies from strong coupling in synoptic trough–ridge environments to weak coupling in quiescent, synoptic ridge environments. Here, we apply an objective dynamic classification of GPLLJ upper-level coupling and fully characterize strongly coupled (C) and relatively uncoupled (UC) GPLLJs from the perspective of the ground-based observer. Through composite analyses of C and UC GPLLJ event samples taken from the European Centre for Medium-Range Weather Forecasts' Coupled Earth Reanalysis of the twentieth century (CERA-20C), we address how the frequency of these jet types, as well as their inherent weather- and climate-relevant characteristics—including wind speed, direction, and shear; atmospheric stability; and precipitation—vary on diurnal and monthly time scales across the southern, central, and northern subregions of the GP. It is shown that C and UC GPLLJ events have similar diurnal phasing, but the diurnal amplitude is much greater for UC GPLLJs. C GPLLJs tend to have a faster and more elevated jet nose, less low-level wind shear, and enhanced CAPE and precipitation. UC GPLLJs undergo a larger inertial oscillation (Blackadar mechanism) for all subregions, and C GPLLJs have greater geostrophic forcing (Holton mechanism) in the southern and northern GP. The results underscore the need to differentiate between C and UC GPLLJs in future seasonal forecast and climate prediction activities.

KEYWORDS: Atmosphere-land interaction; Mesoscale processes; Jets; Hydrometeorology; Diurnal effects

1. Introduction

U.S. Great Plains (GP) low-level jets (GPLLJs) are a predominant source of warm-season climate variability at diurnal to subseasonal time scales. GPLLJ frequencies range from 70% to 97%, 33% to 72%, and 58% to 75% of May–September (MJJAS) nights in the southern Great Plains (SGP), central Great Plains (CGP), and northern Great Plains (NGP), respectively (Burrows et al. 2019a). GPLLJs contribute to nocturnal wind and rainfall maxima (e.g., Helfand and Schubert 1995; Higgins et al. 1997; Yang et al. 2007; Weaver et al. 2009; Hodges and Pu 2018, 2019; Weaver et al. 2012), particularly through their support of mesoscale convective system initiation and maintenance (e.g., Maddox 1983; Squitieri and Gallus 2016a,b; Song et al. 2019), and thus constitute a key weather and climate forecast target.

Important to the prediction and understanding of GPLLJ events, including positioning of their entrance, axis, and exit (convergence) regions, is a recognition that all GPLLJs are not dynamically alike. Dynamical differences between GPLLJs were perhaps first highlighted in a qualitative weather map analysis of Uccellini (1980) that documented a range of GPLLJ vertical coupling to the midlatitude upper-level jet stream. Strongly coupled (C) GPLLJs occur under the influence of upstream troughs/cyclones with stronger upper-atmospheric meridional flow, whereas relatively uncoupled (UC) GPLLJs occur under the presence of local ridges/anticyclones and weak upper-atmospheric flow. A binary classification of GPLLJ vertical coupling was recently automated by Burrows et al. (2019a). Their objective dynamical classification uses the conventional Bonner–Whiteman wind speed and shear criteria (Bonner 1968; Whiteman et al. 1997) to first define spatial coverage of the low-level jet, and subsequently, the local finite-amplitude wave activity diagnostic (Huang and Nakamura 2016) derived from the 500-hPa geopotential height field (i.e., Chen et al. 2015; Martineau et al. 2017), to diagnose coupling according to background synoptic flow patterns (Burrows et al. 2019a). Clear advantages of this approach over previous classification efforts that depended on time-consuming expert analysis (e.g., Wang and Chen 2009; Weng 2000; Walters and Winkler 2001; Mitchell et al. 1995) are its efficiency and reproducibility, which makes it suitable for big data climate applications. Using the European Centre for Medium-Range Weather Forecasts' Coupled Earth Reanalysis of the twentieth century (CERA-20C; Laloyaux et al. 2017, 2018), Burrows et al. (2019a) found statistically significant twentieth-century declines in gridpoint MJJAS UC GPLLJ frequencies, ranging from 0.7 to 3.6 fewer events per decade despite unchanged C GPLLJ frequencies. Because UC GPLLJs tend to transport less moisture, and consequently produce less precipitation over a smaller footprint than C GPLLJs, a reduction in the UC:C GPLLJ event frequency ratio would generally suggest diminished GPLLJ support for drought in the Great Plains. However, the timing or seasonality (i.e., monthly time scales)

Supplemental information related to this paper is available at the Journals Online website: https://doi.org/10.1175/JAS-D-20-0059.s1.

Corresponding author: D. Alex Burrows, burrowswx13@gmail.com

DOI: 10.1175/JAS-D-20-0059.1

of C and UC GPLLJ frequency changes is a critical factor in determining their hydroclimatic impacts.

Given the central role of GPLLJs in modulating regional hydroclimate and in the context of potential ongoing changes to GPLLJ frequency over time (e.g., Cook et al. 2008; Barandiaran et al. 2013; Nikolic et al. 2019), subseasonal UC:C GPLLJ event ratios are deserving of a more careful and complete analysis. Moreover, both C and UC jets, in their own different ways, affect wind energy potential and severe weather generation (e.g., Arritt et al. 1997; Berg et al. 2015; Reif and Bluestein 2017). Thus, there is a need to fully characterize the distinct morphologies of C and UC GPLLJs at spatiotemporal scales that are relevant to weather and climate-related applications and physical process understanding. The objective of this study is to quantify diurnal, monthly, and latitudinal differences between C and UC GPLLJs in order to expand upon previous analyses of jet class MJJAS-mean differences (Burrows et al. 2019a). We address the following specific questions: 1) How do warm-season C and UC GPLLJ frequencies vary as a function of latitude and month? 2) How do their characteristics vary as a function of latitude, time of day, and month? By elucidating the differentiating features of C and UC GPLLJs, this study will highlight the need for future scientists and practitioners to account for GPLLJ vertical coupling. The diurnal and subseasonal time-scale differences will be specifically relevant to short-term severe weather (i.e., extreme wind and precipitation), wind power ramp events, and subseasonal wind and water resources forecasting.

Section 2 provides a description of the data and methodology. Results are presented for GPLLJ frequency analysis and vertical cross section, diurnal, and monthly composite analyses in sections 3a–d, respectively. Section 4 presents a summary and discussion of needed future work.

2. Data and methodology

The analyses herein are focused on a subset of mutually exclusive C and UC GPLLJ events selected from the CERA-20C 110-yr (1901–2010) MJJAS record on the basis of their broad spatial extent and extended duration. Composite analyses of the vertical, longitudinal, diurnal, and subseasonal variabilities are conducted separately for the SGP, CGP, and NGP subregions. Significance of the results is assigned according to 95% bootstrapped confidence intervals (e.g., Ferguson et al. 2018). The following subsections detail the data and methodology more thoroughly.

a. CERA-20C, study region, and period

CERA-20C comprises a 10-member ensemble spanning the period from 1901 to 2010 with 3-hourly output at 1.125° (~125 km) horizontal resolution for 37 pressure levels, 4 soil levels, and the surface. Analyses are limited to the first ensemble member (i.e., ens00), which sufficiently captures the end member C and UC GPLLJ characteristics. CERA-20C native model data were regridded from TL159L91 to regular 1.125° × 1.125° latitude–longitude grids using the now-deprecated ECMWF interpolation library (EMOSLIB, version 4.5.4). Similar to Burrows et al. (2019a), the current study focuses on the 1901–2010 extended summer season (MJJAS) in the context of three 6.75° latitude × 5.625° longitude (i.e., 42 grid) GP subregions. The subregions include the SGP (29.25°–36°N), CGP (36°–42.75°N), and NGP (42.75°–49.5°N)—all spanning 102.375°–96.75°W.

In an analysis of the period from 2001 to 2010, we found CERA-20C's representation of MJJAS-mean GPLLJ characteristics including diurnal cycle, speed, nose height, northern extent, and east–west positioning to be consistent with that of ECMWF's 31-km-horizontal-resolution ERA5 (Hersbach et al. 2020) (not shown). Perhaps the most remarkable difference between the two datasets is that ERA5 places the MJJAS-mean jet nose height at 900 hPa compared to 850 hPa in CERA-20C. While ERA5 spans the period from 1950 to the present, CERA-20C's longer, centennial record provides the larger sample sizes needed to robustly analyze jet class differences at monthly time scales, and thus is the dataset of choice here.

b. Objective dynamically derived GPLLJ classification at a point

Following Bonner (1968) and Whiteman et al. (1997), a GPLLJ is considered incident on a grid point when 1) its 3-hourly total wind speed (V_{max}) exceeds 12 m s^{-1} between the surface and 700 hPa, 2) vertical wind shear (ΔV_z) exceeds 6 m s^{-1} between V_{max} and the minimum wind speed above the pressure level of V_{max} and at or below 700 hPa, and 3) the meridional (i.e., v-wind) component of V_{max} is positive (i.e., southerly). If a GPLLJ is detected for a given gridpoint location and 3-h time step, then an analysis of the regional synoptic flow at 500 hPa is conducted to determine whether the GPLLJ is coupled or uncoupled to the upper-level jet stream. If the strength of the regional anticyclone exceeds a model-specific, climate-based threshold then the grid is assigned an UC GPLLJ classification for that time step. If not, and the strength of the upstream regional cyclone exceeds a similarly defined threshold, then the grid is assigned a C GPLLJ classification for that time step. When neither the local anticyclonic nor upstream cyclonic activity thresholds are exceeded, which tends to occur under zonal flow configurations, the grid is classified as an UC GPLLJ. Complete details of the objective, dynamically derived GPLLJ classification method can be found in Burrows et al. (2019a). However, there is one typo in the methodological description of Burrows et al. (2019a) to note: the upstream cyclonic wave activity search domain as implemented spans the area 16.875° to the west of the jet classification grid not 12.375° as published.

A caveat of the current study is that MJJAS anticyclonic wave activity (AWA) and cyclonic wave activity (CWA) thresholds are applied despite moderate monthly variability in the underlying AWA and CWA time series. For example, CWA is stronger in May and September and relatively weaker in JJA. Hence, applying an MJJAS CWA threshold leads to a slight overestimation of C GPLLJs in May and September and underestimation of C GPLLJs in JJA. Considering that monthly trend analysis is not a focus of the current study, a slight bias in subseasonal event detection was deemed an acceptable trade-off for simplicity and maintenance of the thresholds applied in Burrows et al. (2019a). Interested readers

can access the complete CERA-20C-based GPLLJ upper-level coupling classification dataset for 1901–2010 through the National Center for Atmospheric Research (NCAR) Research Data Archive (Burrows et al. 2019b).

To evaluate the robustness of large-scale dynamical jet classifications based on CERA-20C, we performed an intercomparison with jet classifications derived from NASA's Modern-Era Retrospective Analysis for Research and Applications, version 2 (MERRA-2; Gelaro et al. 2017), over the 31-yr period of overlap between the two datasets (1980–2010). First, MERRA-2 0600 UTC 500-hPa geopotential height (Z500) data at 0.5° latitude × 0.625° longitude resolution was regridded to CERA-20C's 1.125° × 1.125° resolution and MERRA-2-specific MJJAS anticyclonic wave activity and cyclonic wave activity thresholds were calculated. Then, for May–September 1980–2010, following the same methodology used for CERA-20C (see section 2b), each 1.125° × 1.125° grid was classified using CERA-20C wind fields for jet occurrence and upscaled MERRA-2 wave activity thresholds for jet coupling. Over the NGP, CGP, and SGP, there was agreement on 95%, 76%, and 77% of uncoupled GPLLJ gridpoint classifications, respectively. Over the same regions, there was agreement on 31%, 63%, and 82% of coupled GPLLJ gridpoint classifications (Table S1 in the online supplemental material). In summary, the CERA-20C-based dynamical jet classification is generally consistent with that derived from MERRA-2, a modern satellite data reanalysis, except in the case of coupled GPLLJs in the NGP. Many factors could contribute to the observed coupling classification differences, including bias in the underlying wave activity spatiotemporal distribution, which is partly due to the difference in base period used to calculate CERA-20C (1901–2010) and MERRA-2 (1980–2010) wave activity thresholds.

c. *Selection of representative subregional C and UC GPLLJs*

A three-step approach is followed to build samples of indisputably C and UC GPLLJs for each GP subregion. In this new subregional GPLLJ context, an event is defined from 1800 UTC on the day prior to 1500 UTC on the day of the GPLLJ at the subregional scale; however, only qualifying constituent C or UC GPLLJ grids make up the sample. For example, selected MJJAS SGP, CGP, and NGP C GPLLJs make up 11.5, 16.0, and 8.9 grid points out of each subregion's 42 grid points with a standard deviation for event size of 9.7, 9.0, and 8.0, respectively. The remaining grid points with neither a C nor UC GPLLJ incidence are excluded from the composite analyses. The targeted GPLLJs exhibit temporal persistence and spatial uniformity with respect to GPLLJ classification across grids in each subregion. The first step is identifying a candidate day. For a given subregion, 25% or more of the constituent grids must experience the same jet class (C or UC) at 0600 UTC for that day to be considered for inclusion in the subregion's corresponding jet class sample. Once a given day is flagged as a potential GPLLJ day for a given subregion, then an iterative search is carried out to find grids in the subregion for which at least three consecutive 3-hourly time steps, including 0600 UTC (i.e., 0000, 0300, 0600 UTC; 0300, 0600, 0900 UTC; or 0600, 0900, 1200 UTC), have a persistent jet classification (either C or UC) and for which the remaining time steps between 0000 and 1200 UTC (i.e., 0900, 1200 UTC; 0000, 1200 UTC; 0000, 0300 UTC) are not classified as the alternative jet type. The 1800 UTC on day −1 to 1500 UTC on day 0 data from the grids that satisfy this criterion contribute to the corresponding jet class' subregional sample. If a subregional GPLLJ is subsequently found to satisfy both C and UC criteria, then that event day (and all corresponding data) is removed from the analysis; only one type of event—C or UC—may occur in each subregion per day. Complete sample size details are provided in Table 1 in relative terms to the total unfiltered C and UC GPLLJ frequencies during 1901–2010 reported in Burrows et al. (2019a), and event dates are provided in Fig. S1. Notably, zonal shortwave GPLLJs that have been the subject of previous studies (e.g., Tuttle and Davis 2013; Wang et al. 2011) make up less than 4% of GPLLJs on a gridpoint basis (Burrows et al. 2019a) and therefore, are not a focus of the current study.

d. *Composite analyses*

Three composite analyses enable comparison of the vertical, diurnal, and subseasonal characteristics of C and UC GPLLJs, respectively. The first composite analyses are vertical (longitude–pressure) cross sections of the 0600 UTC meridional wind (v-wind), zonal wind (u-wind), and geopotential height (z) taken at the north–south midpoint of each GP subregion, that is, NGP (ϕ = 46.125°N), CGP (ϕ = 39.375°N), and SGP (ϕ = 32.625°N). The second composites cover 3-hourly subregional averages of an array of weather- and climate relevant variables from 1800 UTC on the day prior to the GPLLJ (i.e., day −1) to 1500 UTC on the day of the GPLLJ (i.e., day 0). And the third composites cover 0600 UTC monthly subregional averages of the same variable subset.

Composited variables include 850 hPa total, geostrophic, and ageostrophic wind speeds (W850, $W850_g$, and $W850_a$, respectively) and directions ($W850_{dir}$, $W850_{g,dir}$, and $W850_{a,dir}$, respectively), V_{max}, ΔV_z, height of V_{max} (H_{Vmax}), 0–3-km wind shear (W_{300hPa}–W_{10m}), convective available potential energy (CAPE), convective inhibition (CIN), wind speed at 100 m AGL (W_{100m}), the difference of lifting condensation level (LCL) height and planetary boundary layer (PBL) height (i.e., LCL deficit: H_{LCL}–H_{PBL}), and accumulated precipitation (P). $W850_g$ represents the Coriolis and pressure gradient force balanced portion of W850, while $W850_a$ is the remainder composed of friction from turbulent mixing. $W850_g$ represents the Holton (1967) jet forcing mechanism, whereas $W850_a$ represents the Blackadar (1957) jet forcing mechanism (e.g., Shapiro and Fedorovich, 2010). The following fields are Bonner–Whiteman LLJ criteria: V_{max}, ΔV_z, and H_{Vmax}. W_{300hPa}–W_{10m}, CAPE, and CIN are common severe weather indices; W_{100m} is most relevant to wind energy production, P is critical to quantifying a GPLLJ–hydroclimate relationship; and H_{LCL}–H_{PBL} is a good indicator of potential cloud presence or formation under well-mixed conditions. A negative LCL deficit suggests that clouds are present (e.g., Santanello et al. 2011). W850, W_{300hPa}–W_{10m}, CAPE, CIN, W_{100m}, H_{PBL}, and P are directly output from the reanalysis,

TABLE 1. GPLLJ subregional C and UC jet class sample statistics. The first value is the proportion of days that make up this study's selective C and UC GPLLJ sample sets, which underlies analyses presented in Figs. 2–13. The second value, in parentheses, the proportion of days that make up the total C and UC GPLLJ sample sets (taken from Burrows et al. 2019a; their Fig. 7). All values are in percent (%). For example, 40% of May days between 1901 and 2010 (0.4 × 31 days × 110 years = 1364 days) have a C GPLLJ in the NGP but only 7% of May days (0.07 × 31 days × 110 years = 239 days) are included in the filtered sample.

Region	May	June	July	August	September	MJJAS
C GPLLJ filtered (total) event frequencies (1901–2010)						
NGP	7 (40)	5.7 (33)	4.7 (25)	7.9 (35)	10.1 (42)	6.7 (35)
CGP	22.9 (67)	25.3 (49)	14.7 (28)	21.8 (41)	37.5 (65)	22.8 (50)
SGP	15.8 (30)	6.2 (11)	1.6 (3)	2.2 (4)	9.2 (19)	6.6 (13.4)
UC GPLLJ filtered (total) event frequencies (1901–2010)						
NGP	12.8 (60)	15.3 (67)	20.2 (75)	18.1 (65)	15.1 (58)	15.4 (65)
CGP	7 (33)	19.7 (51)	34.9 (72)	23.3 (59)	9.5 (35)	18 (50)
SGP	35.2 (70)	61.4 (89)	52.1 (97)	39.1 (96)	28.2 (81)	40.8 (86.6)

whereas $V_{\max}$, ΔV_z, $H_{V\max}$, and H_{LCL} are derived quantities. For interested readers, the H_{LCL} calculation details may be found in Ferguson et al. (2012).

In all cases, composites comprise only data from the filtered, quasi-end-member C and UC GPLLJ samples (Table 1) constructed according to the approach described in section 2c. Bootstrap subsampling is used for significance testing with 10 000 bootstraps performed per sample.

3. Results

a. *Warm-season ridge building and low-level southerly winds*

Figure 1 displays the monthly unfiltered climatology of Z500 and 850 hPa v-wind (V850) as well as their daily unfiltered climatology longitudinally averaged over the GP corridor (102.375°–96.75°W). Note the northward May–July then southward July–September migration of Z500 isolines, which marks the northward shift in both the midlatitude jet stream and V850 winds (Figs. 1a,b). In detail, Z500 meridional gradients start out relatively strong for each subregion in May but begin weakening in June over the SGP and by July and August over the CGP and NGP, respectively. In July, the SGP and CGP are dominated by a climatological ridge, while the NGP still experiences relatively stronger gradients. By the end of September, the Z500 meridional gradient structure of May is generally reestablished. Overall, V850 tends to be strongest in the SGP and varies inversely with latitude. It is weakest in the NGP throughout MJJAS. SGP and CGP V850 values peak during JJA, when the Z500 climatology indicates a positive tilted trough—a dynamical setup that impedes upper-level jet coupling (Figs. 1c,d). And in fact, based on a gridpoint-defined GPLLJ, the JJA V850 maximum coincides with peaks in UC GPLLJ frequency (Burrows et al. 2019a; their Fig. 7). Our filtered UC GPLLJ sample (Table 1) is biased toward events in June and July (Figs. 2 and S2).

b. *General characterization of filtered subregional C and UC GPLLJ samples*

Figure 2 displays the subseasonal composition of our C and UC GPLLJ samples for each latitude within the GP, which follows the seasonal frequency statistics of the full GPLLJ samples (i.e., Burrows et al. 2019a, their Fig. 7). UC GPLLJs are more common than C GPLLJs in the SGP and NGP for all months. However, C GPLLJs are more common in the CGP, except during July (Fig. 2c). UC GPLLJ frequency reaches a singular maximum of 45% of days during June over the SGP (Fig. 2a), whereas C GPLLJ frequency has two peaks, one in June (18% of days) and another in September (22% of days)—both over the CGP (Fig. 2b). For each subregion, C GPLLJ frequencies are minimized in July under the influence of a climatological ridge at 500 hPa (Figs. 1a,c). Likewise, C GPLLJ frequency peaks during spring–summer (May–June) and summer–fall (August–September) seasonal transitions concurrent with C GPLLJ associated P maxima (Fig. S3).

Vertical cross-sectional v-wind anomaly composites shown in Fig. 3 clearly differentiate the filtered C and UC GPLLJ vertical coupling conditions from climatology for each subregion. The climatology features an upper-level ridge straddling the GPLLJ's longitudinal axis at approximately 100°W. For each subregion, UC GPLLJ v-wind anomalies tend to reinforce climatological values, whereas C GPLLJ anomalies are out of phase with the climatology. Notably, C GPLLJs have their strongest upper-level (i.e., 500 hPa and above) southerly anomalies within 5°–10° upstream (west) of the GPLLJ (point of maximum low-level southerly anomalies), whereas UC GPLLJ southerly anomalies are strongest 10°–20° upstream of the GPLLJ. This indicates enhanced upper-level support for C GPLLJs through transverse ageostrophic circulations in the exit region of the upper-level jet stream (e.g., Newton 1967; Uccellini 1980). At lower levels (i.e., below 700 hPa), C GPLLJs tend to increase v-winds along the eastern GP representing an eastward shift in the GPLLJ. Overall, throughout the atmospheric column, anomalies are strongest for C (UC) GPLLJ events in the SGP (NGP).

C minus UC GPLLJ composites for v-wind, u-wind, and z are plotted in Fig. 4. Because UC GPLLJ vertical v-wind profiles resemble climatology, the C minus UC GPLLJ difference plots (Figs. 4a–c) are similar to those of Figs. 3a–c. An eastward shift in upper- and lower-level wind differences with increasing latitude is evident. The u-wind (Figs. 4d–f) and z (Figs. 4g–i) differences are generally small at low levels and

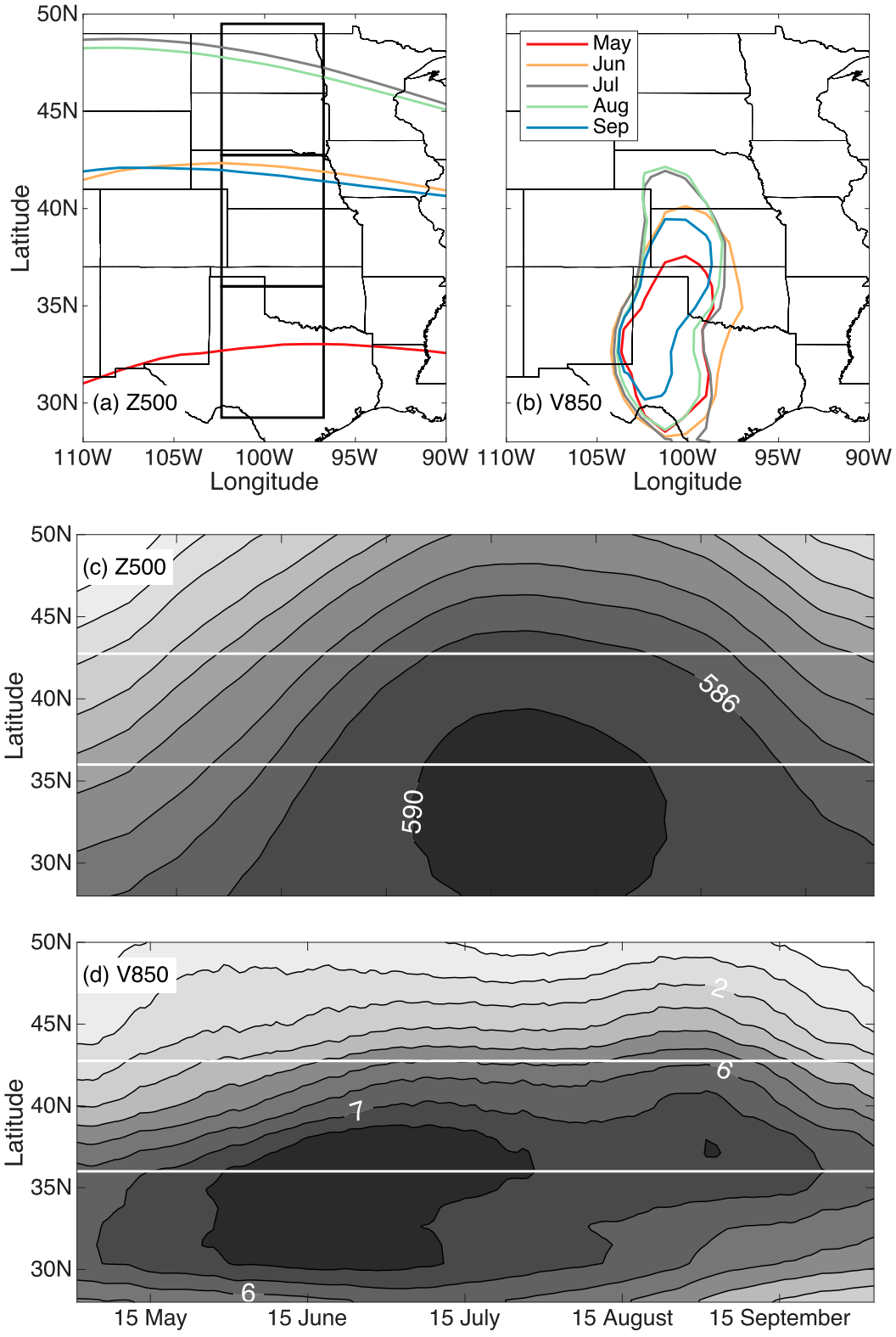

FIG. 1. CERA-20C 1901–2010 monthly mean 0600 UTC (a) 500-hPa 580-dam geopotential height (Z500) and (b) 850-hPa 6 m s^{-1} meridional wind (V850) contours. Hovmöller diagrams (time vs latitude) illustrating the 21-day centered moving average of 0600 UTC (c) Z500 and (d) V850 averaged over the GPLLJ corridor (102.375°–96.75°W), also for the period from 1901 to 2010. Black boxes in (a) and horizontal white lines in (c), (d) demarcate the NGP, CGP, and SGP subregions.

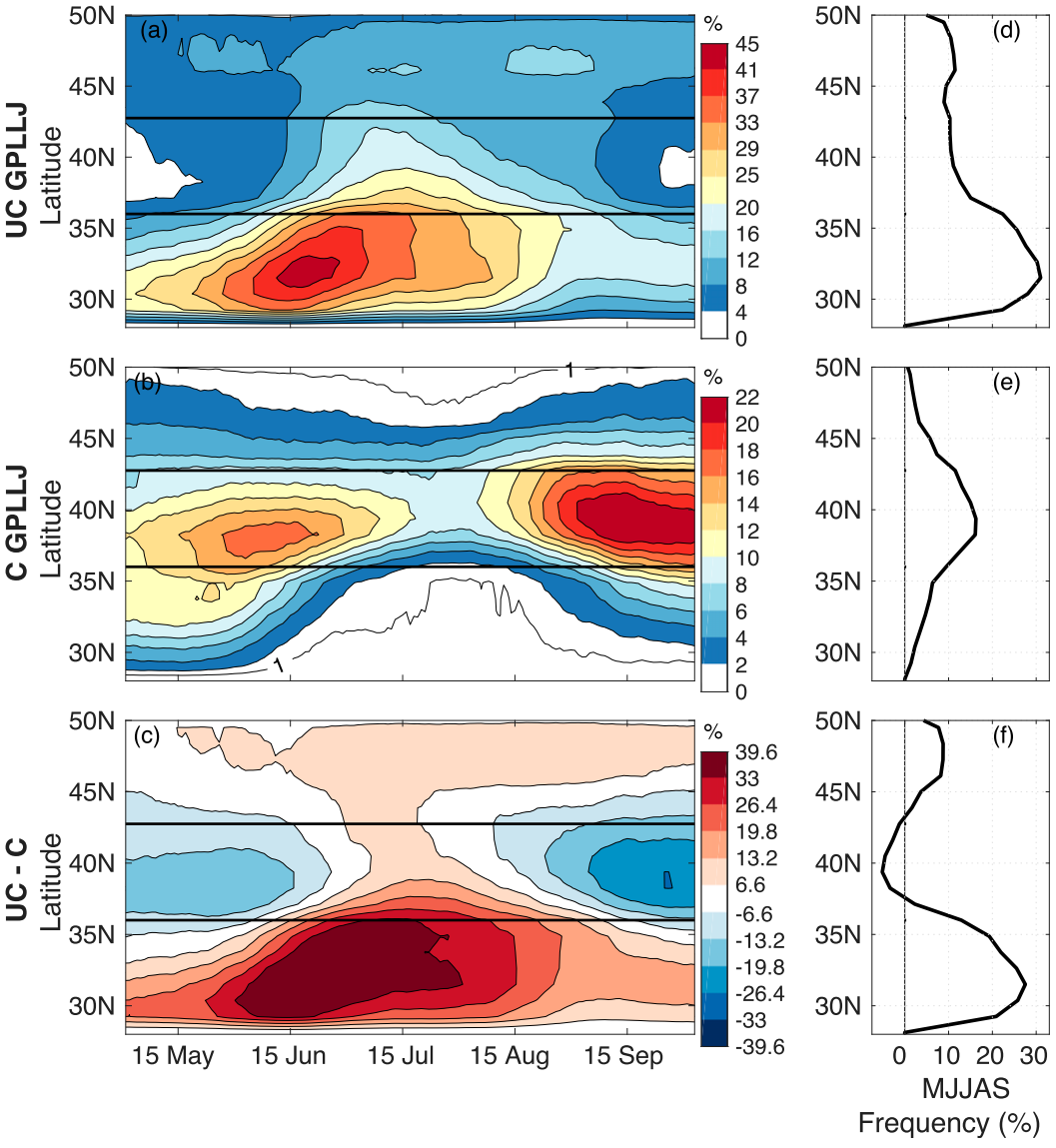

FIG. 2. (left) Hovmöller diagrams illustrating the 21-day centered-moving-average percentage of (a) UC and (b) C GPLLJ grid points in the 6-grid GPLLJ corridor (102.375°–96.75°W), computed from the filtered jet event sample of this study (Table 1). (c) The difference in jet class frequency (UC minus C). (right) The MJJAS-mean frequency of (d) UC, (e) C GPLLJs, and (f) their difference. As in Fig. 1, horizontal lines in (a)–(c) demarcate the CGP subregion. Note that (a) and (b) have different color bar limits. For the corresponding monthly maps of C and UC GPLLJ frequencies, see Fig. S2.

over the GP, but larger at upper levels and upstream. C GPLLJs have stronger upper-level zonal winds associated with domain wide lower z values, particularly west of 100°W. The u-wind differences are particularly strong in the case of GPLLJs over the SGP. Collectively, the v-wind, u-wind, and z difference composites indicate synoptic-scale troughing for the C GPLLJ sample, which is consistent with the dynamical classification applied (section 2b). While UC GPLLJ events will likely have some minimal synoptic support, they will largely be forced by land–atmosphere interactions, including Blackadar (1957) and Holton (1967) jet mechanisms (e.g., Campbell et al. 2019).

c. *Diurnal characterization of filtered subregional C and UC GPLLJ samples*

Diurnal composite analyses are performed on the C and UC GPLLJ filtered samples for an array of weather and climate-relevant variables from 1800 UTC (1300 CDT) on the day prior to the jet to 1500 UTC (1000 CDT) on the day of the jet. Results are presented for the CGP first (Fig. 5), and subsequent figures (Figs. 6–10) highlight regional differences by contrasting SGP and NGP composites. Below, the results discussion is divided into three topical sections: low-level winds, GPLLJ criteria, and atmospheric stability.

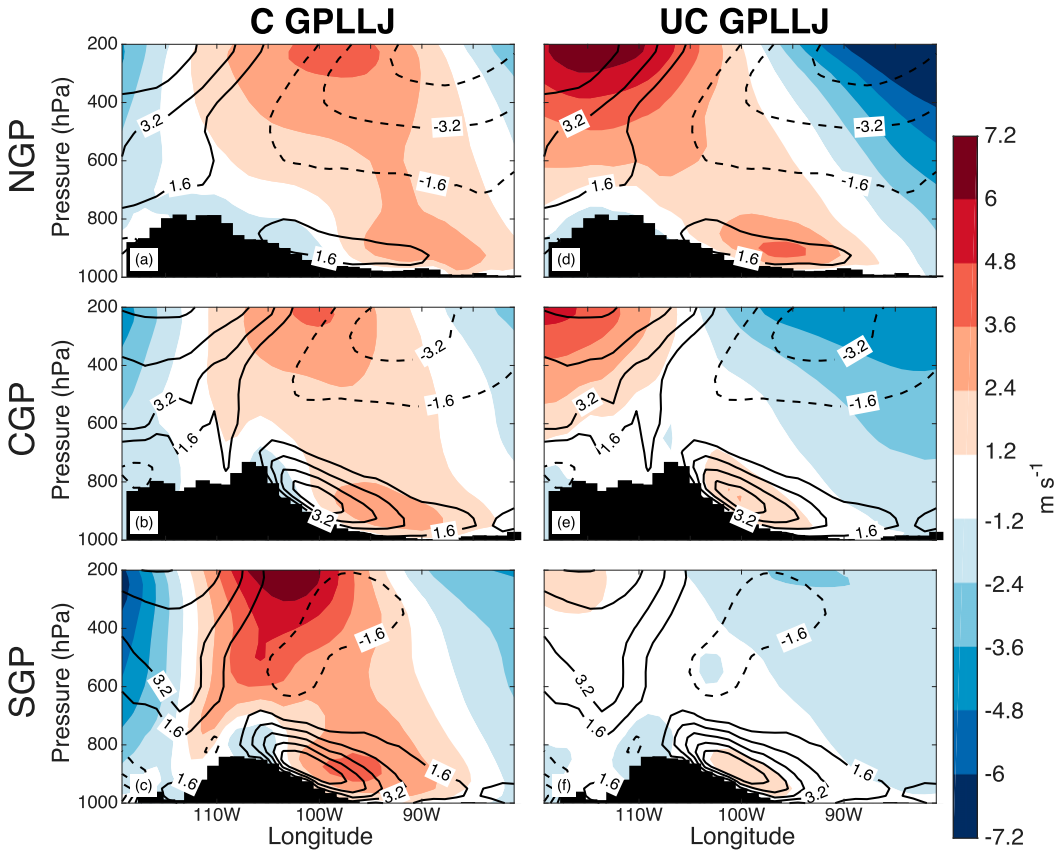

FIG. 3. Composite vertical profiles of the 0600 UTC meridional wind anomalies (color shading) along 120°–80°W corresponding to the total MJJAS (a)–(c) C and (d)–(f) UC GPLLJ conditional sample sets, calculated at (a), (d) 46.125°N, (b), (e) 39.375°N, and (c), (f) 32.625°N (i.e., midpoints of the NGP, CGP, and SGP subregions, respectively). Contours illustrate the meridional wind climatology for all 1901–2010 MJJAS days (including nonjet days). Southerly (negative) wind contours are dashed. Black shading denotes regional surface pressure height.

1) CENTRAL GREAT PLAINS

(i) Low-level winds

Both C and UC GPLLJ W850 progressively increase from late afternoon into the night, maximize at 0600 UTC, and decelerate into midmorning (Fig. 5a). C GPLLJ W850 are significantly stronger than UC GPLLJ W850 between 1800 and 0300 UTC and at 1500 UTC but have a weaker diurnal amplitude. C (UC) GPLLJ W850 values range from 8.3 to 12.4 (from 7.5 to 12.4) m s^{-1}. In general, W850$_g$ explains the majority of W850 magnitude, however, W850$_a$ explains the majority of the diurnal cycle (Figs. 5a–f). C GPLLJ W850$_g$ is nearly constant over the diurnal cycle at 9 m s^{-1}, whereas UC GPLLJ W850$_g$ exhibits a weak but significant diurnal cycle that is out of phase with W850 (i.e., peaking at 10.1 m s^{-1} at 2100 UTC and declining to 8.2 m s^{-1} at 0900 UTC). A similar W850$_g$ diurnal cycle, with marked nocturnal declines, was reported by Parish (2017) in their analysis of UC-like CGP GPLLJs. Late afternoon (2100–0000 UTC) peaks in both C and UC GPLLJ W850$_g$, near the time of nocturnal decoupling of the PBL, is consistent with jet development according to Holton (1967). C and UC GPLLJ W850$_a$ are shown to follow a similar diurnal cycle, although UC GPLLJ W850$_a$ is significantly larger at all times, except 1200–1500 UTC (Fig. 5c). C (UC) GPLLJ W850$_a$ increase from 3.9 (4.3) m s^{-1} at 1800 UTC to 5.8 (6.4) m s^{-1} at 0600 UTC before reducing through midmorning to a minimum of 3.5 (3.3) m s^{-1} at 1500 UTC. Increases in W850$_a$ from 1800 to 0600 UTC can be explained by a loss of daytime surface heat fluxes, which frictionally decouples the boundary layer and free atmosphere leading to a W850$_a$ inertial oscillation (e.g., Blackadar 1957). W850$_a$ values subside from 0600 to 1500 UTC as daytime heating intensifies surface heat fluxes and frictional coupling.

The W850$_{dir}$ and W850$_{g,dir}$ during UC GPLLJs are found to be significantly more westerly than during C GPLLJs, at all hours. However, both the total- and geostrophic winds do share a similar, weak diurnal cycle during both C and UC GPLLJs, rotating anticyclonically from the southwest in the afternoon to slightly more southerly through the night and early morning, which opposes the cyclonic rotation of the inertial oscillation (Figs. 5d,e). The diurnal amplitude of W850$_{a,dir}$ is much more substantial for both jet classes. W850$_a$ rotates from nearly southeasterly at 1800 UTC to southwesterly at 0600 UTC (C: 146°–235°; UC: 115°–259°)

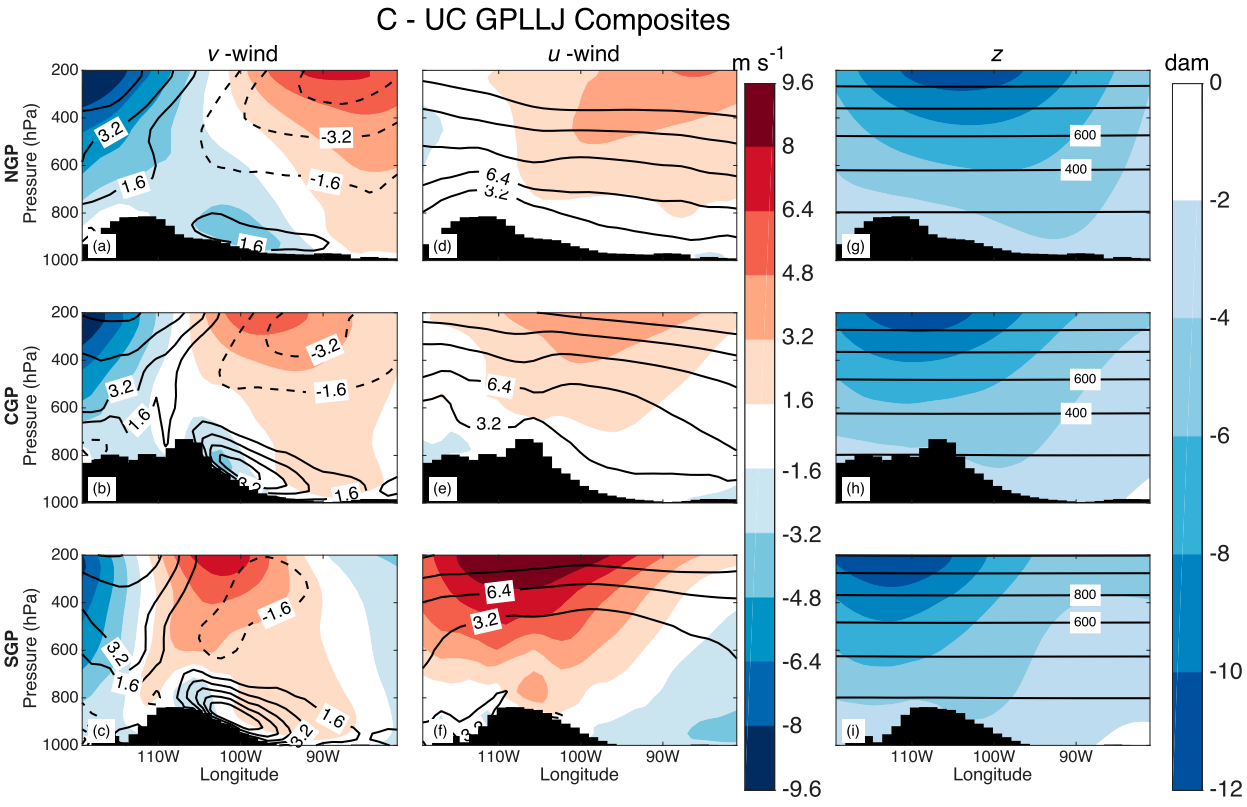

FIG. 4. Composite vertical profiles of the 0600 UTC mean MJJAS difference in (a)–(c) meridional wind (v-wind), (d)–(f) zonal wind (u-wind), and (g)–(i) geopotential height (z) between the C and UC (C minus UC; C − UC) GPLLJ filtered sample sets of this study. Contours illustrate the climatologies for all 1901–2010 MJJAS days (including nonjet days). Dashed contours indicate negative values. As in Fig. 4, composites are taken along the midpoint of (a),(d),(g) NGP, (b),(e),(h) CGP, and (c),(f),(i) SGP. Black shading denotes regional surface pressure height.

and back toward the southeast through midmorning (Fig. 5f). This is a clear indication of an inertial oscillation in the ageostrophic wind field (e.g., Blackadar 1957; Parish 2017), which is shown to have a larger amplitude for UC GPLLJ events. Compared to C GPLLJ W850$_{a,\mathrm{dir}}$, UC GPLLJ W850$_{a,\mathrm{dir}}$ remains significantly more westerly from 0600 to 1500 UTC (Fig. 5f). This suggests that studies that define an LLJ based solely on 850-hPa meridional (i.e., north–south) wind may be underestimating UC GPLLJ frequencies.

(ii) Conventional Bonner–Whiteman GPLLJ criteria

Historically, $V_{\max}$, ΔV_z, and $H_{V\max}$ have been used to categorize and describe GPLLJs (e.g., Whiteman et al. 1997, their Table 1). Figures 5g and 5h show that the phasing of $V_{\max}$ and ΔV_z closely match that of W850 (Fig. 5a), which makes sense considering typical CGP GPLLJ pressure height is approximately 850 hPa. Each jet class's $V_{\max}$ and ΔV_z minimize at 2100 UTC and maximize from 0600 to 0900 UTC (Figs. 5g,h). Although $V_{\max}$ values are significantly stronger for C GPLLJs throughout the diurnal cycle, UC GPLLJs have significantly stronger ΔV_z from 0300 to 1500 UTC; that is, UC GPLLJs are weaker and less temporally consistent, but more strongly sheared. Diurnal amplitudes for both variables are greatest for UC GPLLJs. The $H_{V\max}$ values (Fig. 5i) for both jet classes maximize at 2100 UTC (C: 1670 m; UC: 1363 m AGL), trend lower through the night, and minimize at 0600 UTC (C: 975 m; UC: 725 m AGL). This corresponds to the diurnal evolution of H_{PBL} at CGP (Fig. S4). Depending on wind turbine hub height, which currently ranges from 70 m to over 100 m (e.g., Wiser and Bolinger 2019), the significantly lower UC GPLLJ $H_{V\max}$ could make a large difference in energy production. At 100 m though, the jet class wind speed differences over CGP are marginal (Fig. 5m). Multiple site-specific factors, including C and UC GPLLJ frequencies, $V_{\max}$, $H_{V\max}$, and wind turbine power curves could foreseeably be used to optimize wind energy production and predictability.

(iii) Atmospheric stability

The convective environment associated with C and UC GPLLJs differs significantly. At all times of day, C GPLLJ deep bulk shear ($W_{300\mathrm{hPa}}$–$W_{10\mathrm{m}}$; Fig. 5j) exceeds that of the UC GPLLJ sample by 5.5–6.1 m s^{-1}. Deep bulk shear is relatively constant on a daily time scale for both jet classes. CAPE and CIN, however, both exhibit a substantial diurnal cycle. CAPE minimizes at 1800 UTC (C: 373 J kg^{-1}; UC: 233 J kg^{-1}), maximizes at 0300 UTC (C: 712 J kg^{-1}; UC: 533 J kg^{-1}), and diminishes in the successive hours. C GPLLJ CAPE has a slightly larger diurnal amplitude. It is not surprising that C GPLLJs

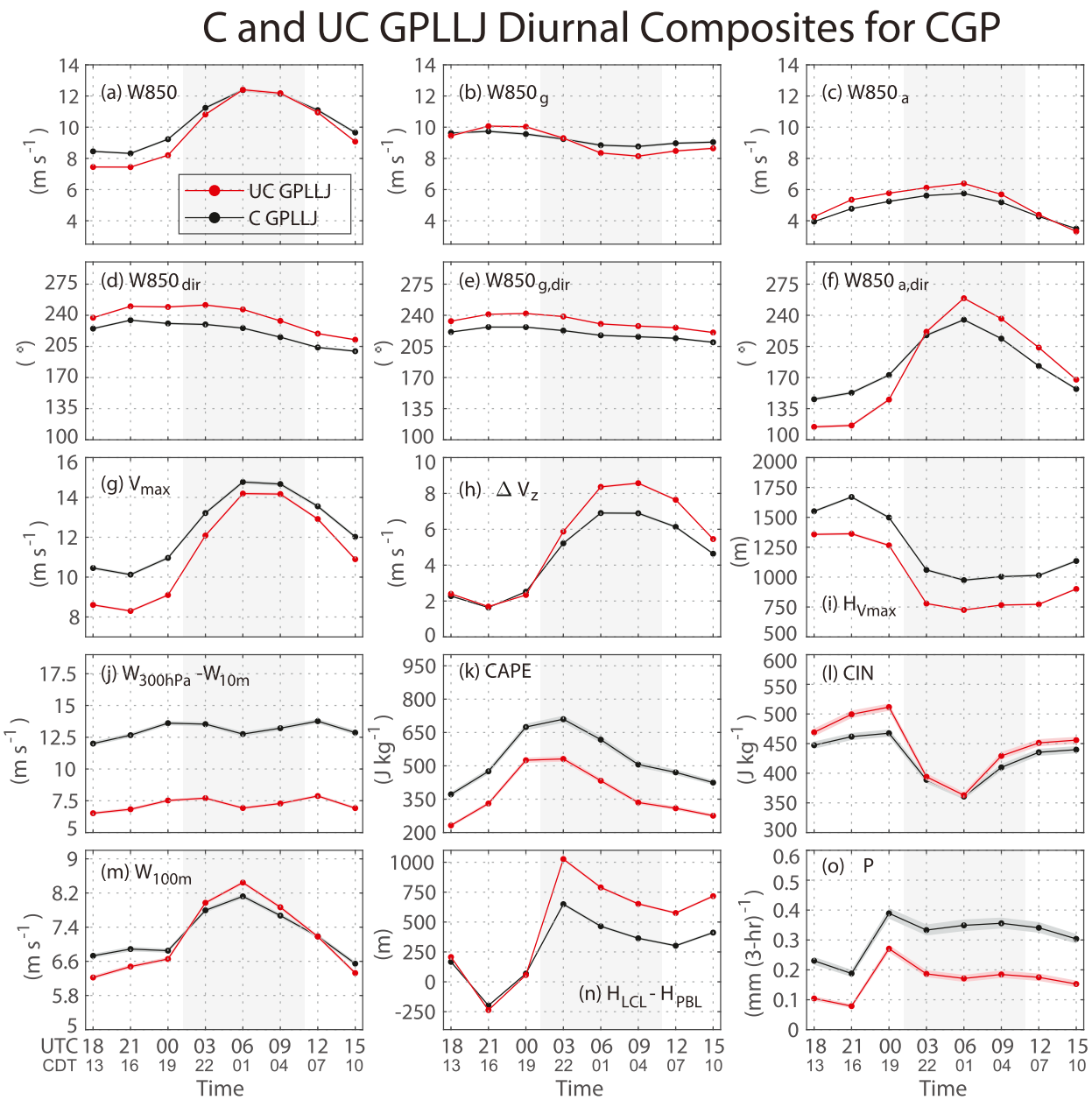

FIG. 5. For the CGP, diurnal composites (i.e., means) of this study's filtered C (black) and UC (red) GPLLJ event subset for (a) 850-hPa wind speed (W850), (b) geostrophic W850 ($W850_g$), (c) ageostrophic W850 ($W850_a$), (d) W850 direction ($W850_{dir}$), (e) $W850_g$ direction ($W850_{g,dir}$), (f) $W850_a$ direction ($W850_{a,dir}$), (g) 1000–700-hPa wind speed maximum (V_{max}), (h) vertical wind shear above the height of V_{max} and at or below 700 hPa (ΔV_z), (i) height of V_{max} (H_{Vmax}), (j) 300-hPa–10-m wind shear (W_{300hPa}–W_{10m}), (k) CAPE, (l) CIN, (m) 100-m wind speed (W_{100m}), (n) difference in height of LCL and height of planetary boundary layer (LCL deficit; H_{LCL}–H_{PBL}), and (o) accumulated precipitation (P). Line widths indicate the 95% bootstrapped confidence interval for each 3-hourly composite value. Light gray background shading indicates nighttime. Wind direction represents the direction wind is coming from (i.e., 180° denotes wind from the south; 270° denotes wind from the west). Note that P is accumulated over the preceding 3 h; all other fields are instantaneous. Corresponding sample size information is provided in Table 1.

have greater deep bulk shear and CAPE given their synoptic setup (Figs. 3, 4) is more favorable for widespread severe weather outbreaks. Peak CIN for both jet classes occur at 0000 UTC. Minimum CIN for both jet classes occur at 0600 UTC (Fig. 5l). C GPLLJ CIN ranges from 361 to 467 J kg^{-1}, whereas UC GPLLJ CIN ranges from 362 to 512 J kg^{-1}. UC GPLLJs have a slightly larger CIN diurnal amplitude due to larger CIN values between 1800 and 0000 UTC leading up to the time of peak precipitation.

The diurnal LCL deficit (H_{LCL}–H_{PBL}) cycles show a significant difference between C and UC GPLLJ samples between

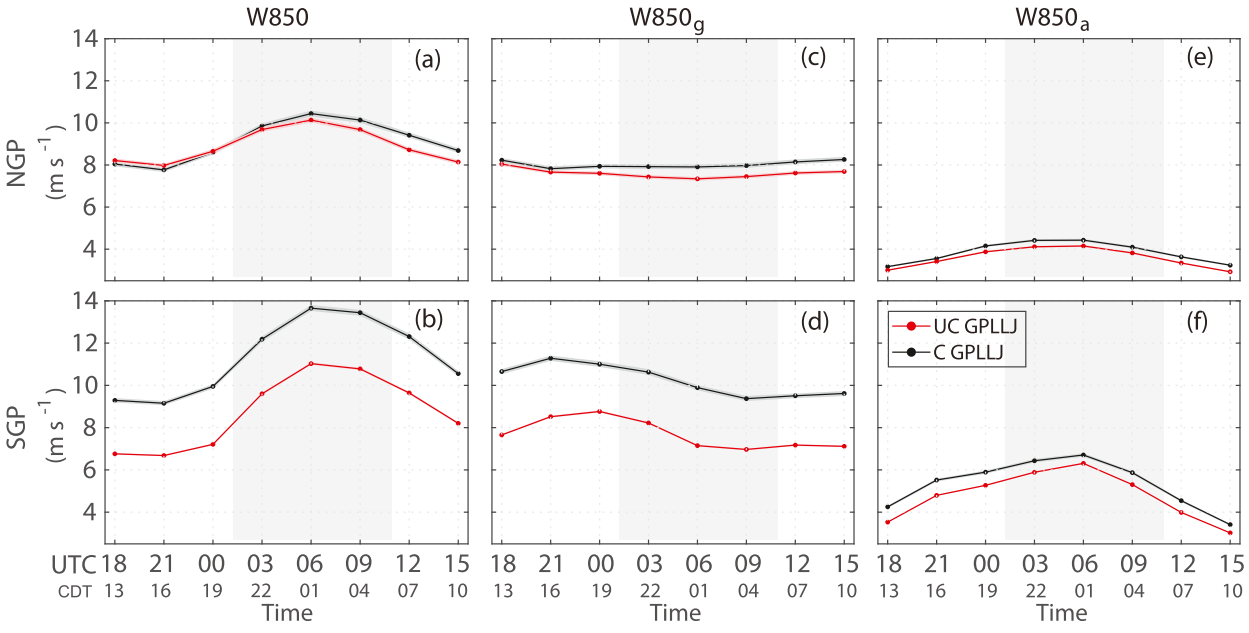

FIG. 6. Diurnal composites of (a),(b) W850, (c),(d) $W850_g$, and (e),(f) $W850_a$ constructed from this study's filtered MJJAS C (black) and UC (red) GPLLJ samples for the (a),(c),(e) NGP and (b),(d),(f) SGP. Line width indicates the 95% bootstrapped confidence interval for each 3-hourly composite value. Light gray background shading indicates nighttime.

0300 and 1500 UTC, during which time UC GPLLJs have a markedly larger LCL deficit (304 m at 1500 UTC; Fig. 5n). LCL deficit is negative or near zero for both jet classes between 1800 and 0000 UTC, which suggests a strong potential for cloud development. Consistent with reduced LCL deficits, precipitation accumulation (P) for both jet classes maximize at 0000 UTC (i.e., the 2100–0000 UTC accumulation). Also, consistent with significantly lower C GPLLJ LCL deficits from 0300 to 1500 UTC, P during C GPLLJs is larger (Fig. 5d). P values remain fairly constant in the hours following 0000 UTC maxima [C: 0.39 mm $(3\,h)^{-1}$; UC: 0.27 mm $(3\,h)^{-1}$] for both jet classes with the C GPLLJ sample averaging 0.16 mm $(3\,h)^{-1}$ more P from 0300 to 1500 UTC.

2) SGP VERSUS NGP CONTRASTS

In Figs. 6–10, we draw out the latitudinal differences in C and UC GPLLJ morphology by contrasting SGP and NGP diurnal cycle composites for each of the variables of interest considered in our preceding CGP analysis (Fig. 5). Starting with W850, Figs. 6a and 6b show similar results over SGP and NGP as compared to CGP. For both jet classes, W850 minimizes at 2100 UTC, maximizes at 0600 UTC and weakens through midmorning. C GPLLJ W850 values are as strong or stronger than comparative UC GPLLJ values at each time step and for each subregion. This is particularly true in the SGP where values are 2.2–3.0 m s^{-1} greater throughout the diurnal cycle. In contrast to the CGP results, C GPLLJ $W850_g$ (Figs. 6c,d) and $W850_a$ (Figs. 6e,f) are stronger than UC GPLLJ values at all times. The three-hourly maximum W850, $W850_g$, and $W850_a$ each decrease from south to north for both jet classes. Likewise, their diurnal amplitudes and C − UC GPLLJ differences progressively decrease from SGP to CGP to NGP.

The $W850_{dir}$, $W850_{g,dir}$, and $W850_{a,dir}$ diurnal cycles at SGP and NGP for both jet classes are consistent with those shown for CGP. That is to say, UC GPLLJ $W850_{dir}$ (Figs. 7a,b) and $W850_{g,dir}$ (Figs. 7c,d) are consistently more westerly relative to C GPLLJ values throughout the day, and both fields exhibit very little diurnal variability. The $W850_{a,dir}$ diurnal amplitudes decrease from SGP (C: 120°; UC: 159°) to CGP (C: 89°; UC: 140°) and, finally, NGP (C: 65°; UC: 75°) (Figs. 7e,f). The decline in UC GPLLJ $W850_{a,dir}$ diurnal amplitude from CGP to NGP is particularly remarkable. Summarizing, although inertial oscillation timings are similar across the GP subregions, the SGP (NGP) experiences the strongest (weakest) inertial oscillation.

Previous studies (e.g., Jiang et al. 2007; Shapiro et al. 2016) have demonstrated that both Blackadar and Holton mechanisms must be operative in order to realistically simulate GPLLJs but the potential influence of upper-level jet coupling on the relative balance of these two mechanisms has not yet been addressed. Here, we explicitly show the degree to which Holton and Blackadar mechanisms are operative in C and UC GPLLJs through an analysis of $W850_g$ and $W850_a$. For all GP subregions and for both C and UC GPLLJs, $W850_g$ maxima occur between 1800 and 0000 UTC (Figs. 5b, 6c,d). C (UC) GPLLJ $W850_g$ is largest for the SGP (CGP), indicating a stronger Holton forcing for that jet class and subregion. The relative strength of Blackadar mechanistic forcing may be judged on two characteristics: 1) the time $W850_a$ rotation begins and 2) the amplitude of this rotation. CGP and NGP (SGP) C and UC GPLLJ $W850_a$ begin rotating clockwise at 1800 (2100) UTC and reach a maximum westerly component at 0600 UTC. For the SGP and CGP, both jet class W850 become supergeostrophic (i.e., W850 > $W850_g$) between 0000 and

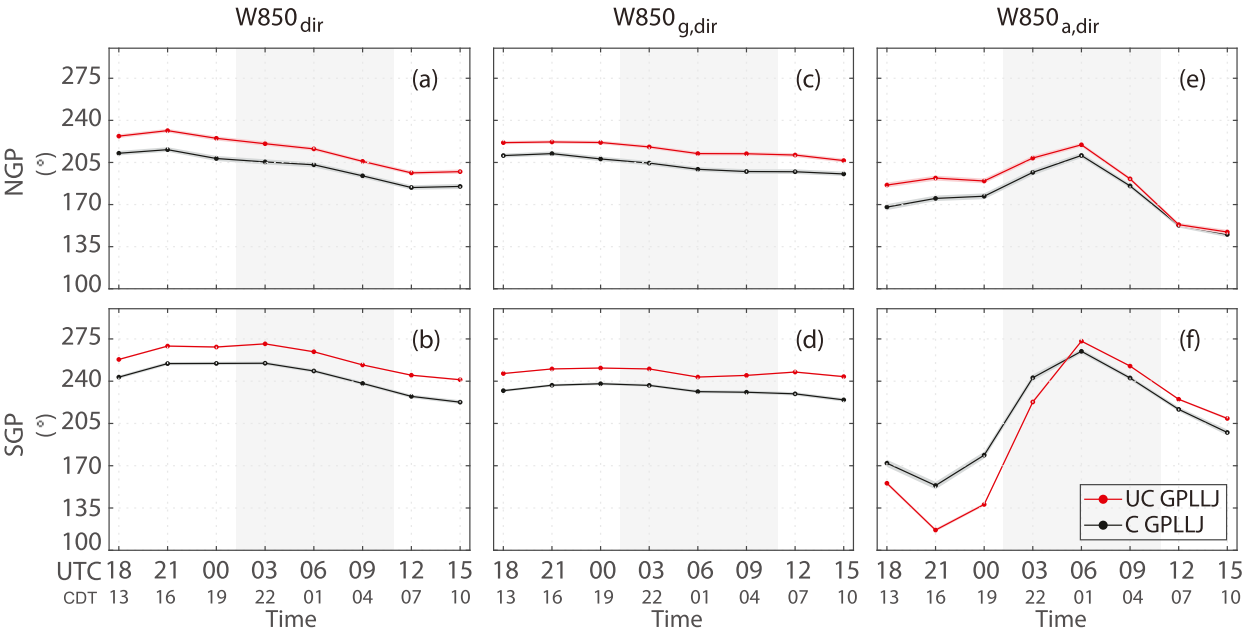

FIG. 7. As in Fig. 6, but for (a),(b) $W850_{dir}$, (c),(d) $W850_{g,dir}$, and (e),(f) $W850_{a,dir}$.

0300 UTC, whereas for the NGP, C GPLLJ supergeostrophic winds begin between 2100 and 0000 UTC, and UC GPLLJs are supergeostrophic throughout the day. Rotation amplitudes maximize for the SGP (C: 120°; UC: 159°) and minimize for the NGP (C: 65°; UC: 75°). This SGP maximum may be explained by maxima in W850 and V_{max} accelerations into the night, suggesting the SGP is strongly affected by the Blackadar mechanism.

Similar to findings for CGP, W_{100m} for SGP and NGP minimizes in late afternoon and peaks at 0600 UTC (Figs. 10a,b). The diurnal W_{100m} composites differ insignificantly between jet classes for the NGP, as is the case of several time steps for the SGP (Figs. 5m, 10a). However, the separation between C and UC GPLLJ W_{100m} broadens for the SGP, where C GPLLJ W_{100m} exceed comparative UC GPLLJ values by 1.1 m s^{-1} on average.

The V_{max} and ΔV_z diurnal cycles for SGP and NGP generally convey the same message—that diurnal amplitude, as well as the magnitude of differences between C- and UC-derived diurnal values, decrease from south to north. Relatedly, daily averaged C GPLLJ V_{max} exceed UC GPLLJ values by 2.8, 1.2, and 0.4 m s^{-1} for the SGP, CGP, and NGP, respectively. H_{Vmax} for both jet class samples are found to increase marginally from SGP to CGP to NGP across all time steps, and perhaps most importantly, at nighttime when V_{max} peaks (Fig. 8).

In terms of atmospheric stability, W_{300hPa}–W_{10m} is found to average 5.5 m s^{-1} greater in C GPLLJs, considering all time steps and subregions. Both C and UC GPLLJ W_{300hPa}-W_{10m} daily mean values increase moving south to north (Figs. 9a,b). Diurnal composites of CAPE at SGP are similar to those for CGP. The maximum and minimum SGP CAPE values occur at 0000 and 0900 UTC, respectively, for both jet classes. And SGP CAPE is greater during C GPLLJs at all times of the day (Fig. 9d). By contrast, the NGP CAPE diurnal amplitude is smaller, with a broader maximum from 0000 to 0600 UTC, and the interjet class spread is negligible. Besides a few time steps in the CGP (Fig. 5l) and NGP (Fig. 9e) when interjet class differences are insignificant, UC GPLLJ CIN exceeds that of C GPLLJs for each subregion, and both jet classes maximize (minimize) at 1800–0000 (0300–0600) UTC. For example, UC GPLLJ maximum 3-hourly CAPE values (i.e., at 0300 UTC) are 147 and 77 J kg^{-1} larger in NGP than in SGP and CGP, respectively.

Consistent with findings for the CGP, the LCL deficit is found to minimize at 2100 UTC and maximize at 0300 UTC. Early morning (1200–1500 UTC) UC GPLLJ LCL deficits exceed those of C events across each subregion, whereas late afternoon (1800–0000 UTC) jet class LCL deficit differences are insignificant (Figs. 6n, 10c,d). Similar to the diurnal P cycle at CGP, P is found to maximize at 0000 UTC for both jet classes in the SGP and for UC GPLLJs in the NGP. However, in the NGP, C GPLLJ P peaks in the early morning (1200 UTC). The difference between C and UC GPLLJ P diurnal cycles diminishes progressively from SGP to CGP to NGP.

d. Subseasonal characterization of filtered subregional C and UC GPLLJ samples

An analysis of the same variable fields considered previously at 3-hourly time scales (Figs. 5–10) is conducted at monthly time scales using data from 0600 UTC when V_{max} is maximized. Based on results from the preceding diurnal cycle analysis, the sign of C and UC GPLLJ differences at 0600 UTC will be representative of all times of day, except for $W850_{a,dir}$, for which the sign of differences will be reversed from 1800 to 0000 (1800 to 0300) UTC for CGP (SGP). Three specific questions

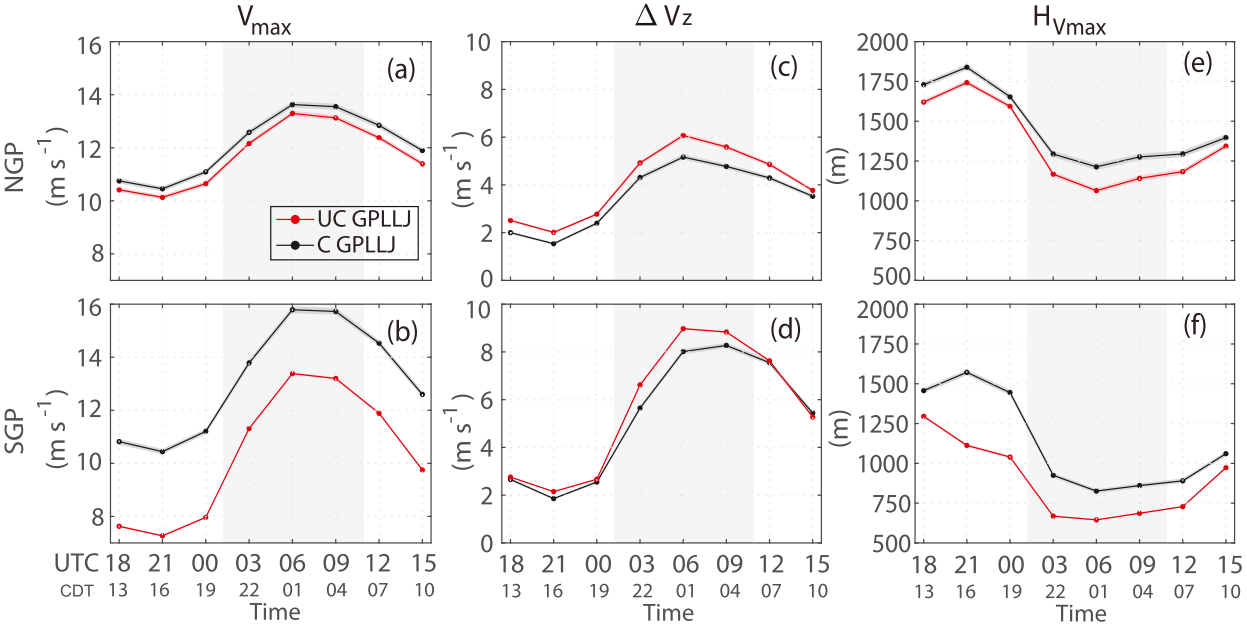

FIG. 8. As in Fig. 6, but for (a),(b) V_{max}, (c),(d) ΔV_z, and (e),(f) H_{Vmax}.

are addressed: 1) What is the relative seasonality of each of the considered parameter fields? 2) How does this seasonality differ between C and UC GPLLJ conditioned samples? 3) During which months are C and UC GPLLJ sample differences greatest? Following the layout of the preceding section 3c, results will be presented for the CGP first, followed by a reporting of the comparative differences between SGP and NGP results. Table 2 provides a summary of the corresponding monthly statistics.

1) CENTRAL GREAT PLAINS

(i) Low-level winds

C and UC GPLLJ W850, $W850_g$, and $W850_a$ exhibit moderate seasonality. Monthly W850 ranges from 11.1 to 13.4 m s^{-1} for C GPLLJ and 11.7 to 13.2 m s^{-1} for UC GPLLJ samples. Both jet types have stronger winds in May–June and weaker winds in July–August (Figs. 11a–c). The only significant differences between jet types were found in June–July for W850 and May for $W850_g$. By

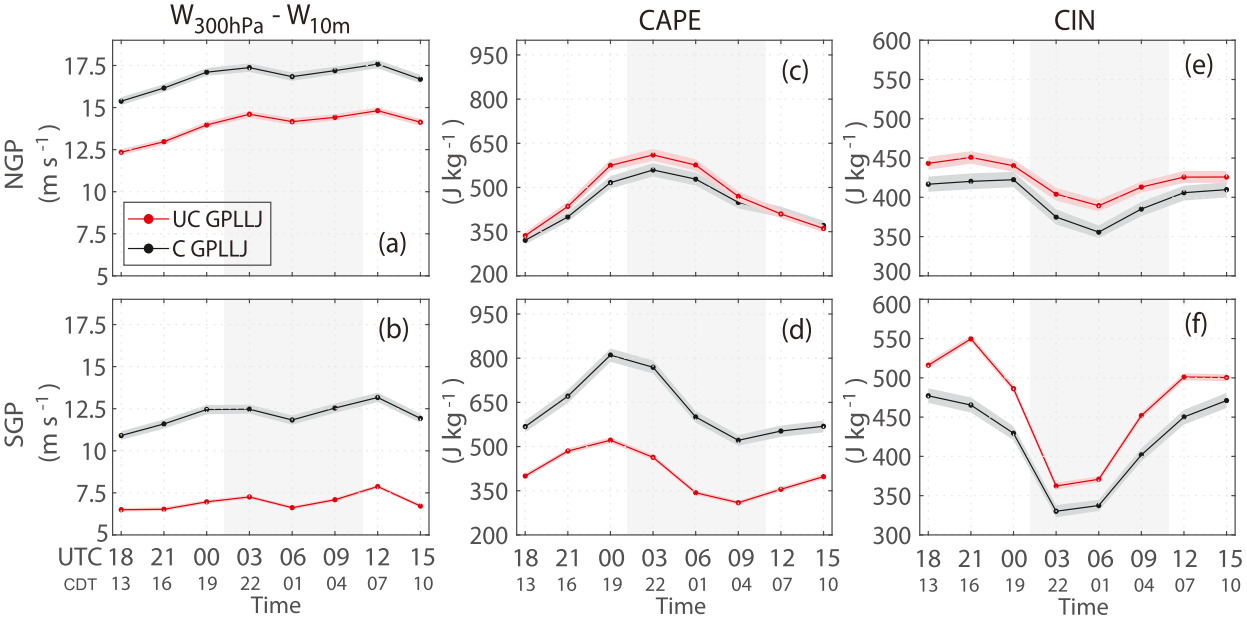

FIG. 9. As in Fig. 6, but for (a),(b) W_{300hPa}–W_{10m}, (c),(d) CAPE, and (e),(f) CIN.

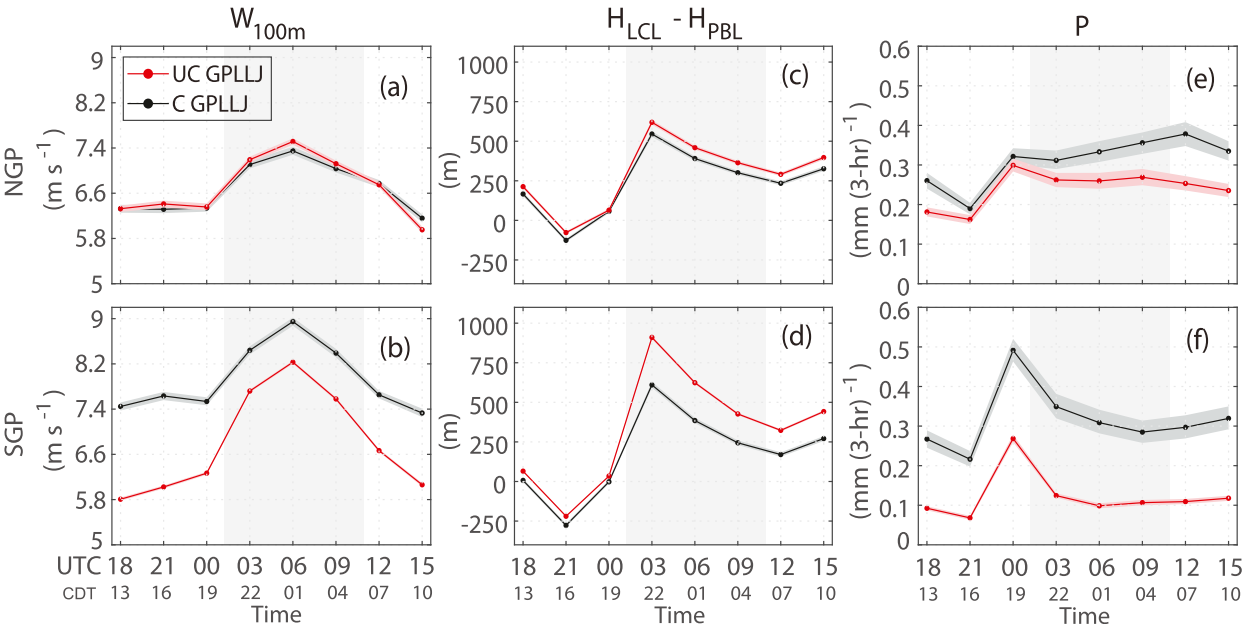

FIG. 10. As in Fig. 6, but for (a),(b) W_{100m}, (c),(d) H_{LCL}–H_{PBL}, and (e),(f) P.

contrast, interjet class differences in W850$_a$ were significant for all months. UC GPLLJ W850$_a$ is on average 0.64 m s^{-1} faster relative to the C GPLLJ W850$_a$ for all months (Fig. 11c). C and UC GPLLJ W_{100m} follow the same seasonal cycle as W850. UC GPLLJ W_{100m} is greater by 0.4 m s^{-1} on average (Fig. 11m).

C GPLLJ W850$_{dir}$ is nearly constant at 225° (southwesterly) throughout MJJAS, whereas UC GPLLJ W850$_{dir}$ is 234° in May and experiences a moderate 6.6° month^{-1} rotation farther westerly between May and August before rotating back easterly in September (Figs. 11d–f). On average, UC GPLLJ W850$_{dir}$ is 14° west of C GPLLJ W850$_{dir}$. C (UC) GPLLJ W850$_{dir}$ and W850$_{g,dir}$ exceed (i.e., are more westerly) MJJAS-mean values in June/August (July–August), while C (UC) GPLLJ W850$_{a,dir}$ exceed MJJAS-mean values in August (July–August). Maximum C (UC) W850$_{a,dir}$ occur in August at 245° (267°). Each C and UC GPLLJ wind component has similar MJJAS-seasonal amplitudes.

(ii) Conventional Bonner–Whiteman GPLLJ criteria

C and UC GPLLJ V_{max} monthly means range from 13.5 to 15.3 m s^{-1} and from 13.4 to 14.4 m s^{-1}, respectively, with larger values in May–June and lower values in July–August. Interjet class differences are only significant in May–June and September when C GPLLJ values are larger (Fig. 11g). UC GPLLJ ΔV_z exceed C GPLLJ ΔV_z values by 0.3 m s^{-1} throughout MJJAS (Fig. 11h). Both C and UC GPLLJ ΔV_z minimize in May, increase by ~1.3 m s^{-1} and hold nearly constant from June to September. C (UC) GPLLJ $H_{V\max}$ ranges from 860 to 1098 (from 675 to 873) m. C GPLLJ $H_{V\max}$ is larger than UC GPLLJ $H_{V\max}$ by 178–249 m (Fig. 11i). Both jet class's ΔV_z and $H_{V\max}$ have weak seasonal cycles.

(iii) Atmospheric stability

C and UC GPLLJ monthly bulk shear (W_{300hPa}–W_{10m}) varies from 11.0 to 14.9 and from 5.6 to 9.8 m s^{-1}, respectively, over MJJAS (Fig. 11j). Both jet classes exhibit the greatest bulk shear in May and September, least bulk shear in July–August and have similar but weak bulk shear seasonal amplitudes. C GPLLJ bulk shear exceeds UC GPLLJ shear, consistent with stronger upper-level flow for C GPLLJ events (Figs. 3, 4). Bulk shear follows closely to the seasonal migration of Z500, that is, weakest shear values in July coincide with the weakest Z500 gradients (Figs. 1a,c). Monthly C and UC GPLLJ CAPE maximizes in June for both jet classes (C: 1097 J kg^{-1}; UC: 751 J kg^{-1}) and declines linearly from June through to September minima (C: 316 J kg^{-1}; UC: 235 J kg^{-1}; Fig. 11k). Besides May, C GPLLJ CAPE is substantially larger than UC GPLLJ CAPE and relatedly, has a larger seasonal amplitude. C and UC GPLLJ CIN follow a similar seasonal cycle to CAPE including an increase from May values to June maxima and subsequent steady decline through August. However, unlike CAPE, CIN slightly increases from August to September (Fig. 11l). C and UC GPLLJ CIN are insignificantly different besides in May when UC GPLLJ CIN is 65 J kg^{-1} larger.

The seasonal amplitude of LCL deficit is fairly large for both jet classes and can be explained by a climatological decrease in near-surface relative humidity from May to August and rebound from August to September (not shown). Both jet class's LCL deficits minimize in May (C: 113 m; UC: 365 m), increase from May to maxima in August (C: 733 m; UC: 973 m), and reduce slightly into September. The difference in LCL deficit between C and UC GPLLJs is 230–300 m throughout MJJAS. C and UC GPLLJ P and LCL deficit seasonal cycles are anticorrelated (Fig. 11o). Both jet class P values maximize in May with C (UC) GPLLJ P minimizing in August (July). C GPLLJ P ranges from 0.06 to 0.20 mm (3 h)$^{-1}$ greater than UC GPLLJ P (Fig. 11o). UC GPLLJs are associated with lower soil moisture values, particularly in the CGP (Fig. S5). Confirming

TABLE 2. GPLLJ subregional C and UC jet class sample 0600 UTC monthly mean, monthly standard deviation, monthly maximum, and monthly minimum statistics for May–September during 1901–2010 from CERA-20C. These statistics correspond to Figs. 11–13.

		MJJAS mean (monthly standard deviation)			MJJAS monthly maximum (minimum)		
Variable	Class	SGP	CGP	NGP	SGP	CGP	NGP
W850 ($m\,s^{-1}$)	C	13.2 (1.4)	12.3 (1.0)	10.4 (0.6)	15.1 (11.5)	13.4 (11.1)	11.0 (9.6)
	UC	11.0 (0.7)	12.5 (0.7)	10.3 (0.7)	11.9 (10.2)	13.2 (11.7)	11.0 (9.5)
$W850_g$ ($m\,s^{-1}$)	C	9.4 (1.3)	8.7 (1.1)	7.9 (0.8)	11.2 (8.0)	10.0 (7.4)	8.9 (6.9)
	UC	7.2 (1.0)	8.5 (0.8)	7.5 (0.8)	8.2 (6.0)	9.2 (7.5)	8.5 (6.6)
$W850_a$ ($m\,s^{-1}$)	C	6.5 (0.7)	5.7 (0.3)	4.4 (0.01)	7.4 (5.7)	6.2 (5.5)	4.6 (4.3)
	UC	6.3 (0.3)	6.4 (0.2)	4.1 (0.01)	6.7 (6.0)	6.7 (6.2)	4.3 (4.0)
$W850_{dir}$ (°)	C	251.0 (5.6)	226.0 (5.8)	203.8 (6.5)	257.6 (243.6)	231.9 (219.6)	210.4 (195.0)
	UC	263.4 (8.2)	244.3 (8.4)	216.5 (3.9)	271.6 (251.3)	253.8 (232.6)	220.9 (210.8)
$W850_{g,dir}$ (°)	C	234.8 (6.6)	217.6 (5.3)	199.9 (6.2)	242.5 (228.2)	225.3 (212.3)	208.0 (192.2)
	UC	242.3 (8.7)	228.6 (6.2)	212.9 (3.6)	250.6 (232.2)	234.9 (219.9)	217.2 (209.9)
$W850_{a,dir}$ (°)	C	267.3 (8.4)	235.2 (4.9)	211.0 (4.7)	278.2 (255.0)	242.5 (228.9)	217.4 (204.2)
	UC	272.7 (8.3)	257.1 (9.6)	219.7 (3.2)	280.1 (258.9)	266.3 (241.9)	223.5 (215.4)
V_{max} ($m\,s^{-1}$)	C	15.3 (1.4)	14.7 (1.2)	13.5 (0.6)	17.1 (13.6)	15.8 (13.3)	14.4 (12.8)
	UC	13.4 (0.9)	14.4 (0.8)	13.4 (0.6)	14.4 (12.5)	15.2 (13.3)	14.2 (12.7)
ΔV_z ($m\,s^{-1}$)	C	8.5 (1.0)	6.9 (0.7)	5.1 (0.5)	9.4 (6.8)	7.4 (5.7)	5.8 (4.7)
	UC	8.9 (0.5)	8.3 (0.6)	6.1 (0.2)	9.6 (8.5)	8.7 (7.3)	6.3 (5.9)
H_{Vmax} (m)	C	782.3 (108.0)	968.9 (88.3)	1213.2 (58.2)	955.4 (669.6)	1098.4 (860.3)	1275.3 (1130.2)
	UC	649.4 (64.7)	744.1 (80.3)	1065.2 (34.5)	756.5 (589.9)	873.0 (675.3)	1116.4 (1027.0)
W_{300hPa}–W_{10m} ($m\,s^{-1}$)	C	9.4 (5.0)	12.5 (1.7)	16.7 (0.8)	16.3 (4.5)	14.9 (11.0)	17.9 (15.8)
	UC	7.0 (3.8)	7.5 (1.8)	14.2 (0.6)	12.5 (3.5)	9.8 (5.6)	14.8 (13.2)
CAPE ($J\,kg^{-1}$)	C	533.4 (263.4)	645.5 (295.2)	570.1 (319.4)	874.0 (301.2)	1097.3 (316.1)	974.8 (247.9)
	UC	346.3 (233.1)	440.3 (215.3)	549.6 (310.1)	669.0 (142.9)	750.9 (234.9)	903.1 (228.0)
CIN ($J\,kg^{-1}$)	C	341.9 (29.5)	361.1 (36.0)	348.7 (67.4)	384.3 (309.9)	401.6 (305.8)	393.8 (233.3)
	UC	363.3 (60.7)	363.8 (30.1)	380.0 (53.3)	427.3 (288.4)	407.7 (326.0)	425.2 (288.8)
W_{100m} ($m\,s^{-1}$)	C	8.8 (0.6)	8.1 (0.4)	7.3 (0.3)	9.7 (8.1)	8.5 (7.7)	7.7 (6.9)
	UC	8.2 (0.4)	8.5 (0.3)	7.6 (0.3)	8.7 (7.8)	8.8 (8.1)	7.9 (7.3)
H_{LCL}–H_{PBL} (m)	C	457.2 (199.9)	473.1 (256.2)	368.0 (246.6)	685.8 (164.1)	732.8 (113.1)	631.9 (64.2)
	UC	613.0 (240.8)	734.9 (249.8)	425.7 (239.7)	877.9 (270.1)	973.2 (364.5)	682.0 (124.1)
P [mm ($3\,h^{-1}$)]	C	0.3 (0.1)	0.3 (0.1)	0.4 (0.2)	0.4 (0.1)	0.5 (0.2)	0.6 (0.2)
	UC	0.1 (0.04)	0.2 (0.1)	0.3 (0.1)	0.2 (0.1)	0.3 (0.1)	0.5 (0.1)

the causality of the GPLLJ-soil moisture correlations, that is, the extent to which soil moisture determines jet class frequency, or vice versa, would require additional idealized modeling studies that are beyond the scope of this study.

2) SGP VERSUS NGP CONTRASTS

Consistent with findings at the diurnal time scale, differences between C and UC GPLLJ characteristics increase from north to south (i.e., the largest spread is found in SGP), except in the case of $W850_{a,dir}$, ΔV_z, H_{Vmax}, and W_{300hPa}–W_{10m}, for which the interjet class differences are greatest in the CGP. Generally, jet class–related differences are largest during May–June and smallest during July–August (e.g., $W850_g$, $W850_a$, V_{max}, ΔV_z, H_{Vmax}, CIN, CAPE, W_{100m}, and P; Figs. 11–13, Figs. S6–S8, and Table 2). Although, the C and UC GPLLJ sample derived means differ insignificantly for several variable/month cases (e.g., May–June and September CGP W850; July–August CGP V_{max}; and June–September CGP CIN; Fig. 11), especially in the NGP (Figs. S6–S9). In terms of seasonality, C and UC GPLLJ sample monthly means cover similar ranges in the CGP and NGP. However, C GPLLJ variables exhibit substantially greater monthly variability in the SGP. An important caveat to that statement is that C GPLLJs are relatively uncommon in the SGP, particularly in July–August (Table 1). Accordingly, the underlying sample size is small and the confidence interval broad. One final interesting observation is that while monthly C and UC GPLLJ ΔV_z is nearly constant during June–September in NGP, it is substantially lower in May for C GPLLJ events in both CGP and SGP (Figs. 11g and S6c,d).

4. Summary and discussion

The research community has long acknowledged that GPLLJs vary in their degree of upper-level atmospheric coupling (e.g., Uccellini 1980; Wang and Chen 2009; Walters and Winkler 2001; Walters 2001; Frye and Mote 2010). Due to limited sample sizes and largely subjective (e.g., visual) diagnostic approaches, past comparative analyses of strongly C and weakly C or UC jet classes have tended to be more qualitative than quantitative. The objective GPLLJ dynamic classification framework introduced by Burrows et al. (2019a) is the first to make detailed, large-sample, quantitative comparisons of C and UC GPLLJs feasible. Burrows et al. (2019a) demonstrated the application of their framework in a quantification of large-scale, seasonal mean (i.e., May–September) differences between C and UC GPLLJs using CERA-20C. However, this study was needed to further characterize differences between C and UC GPLLJs at diurnal

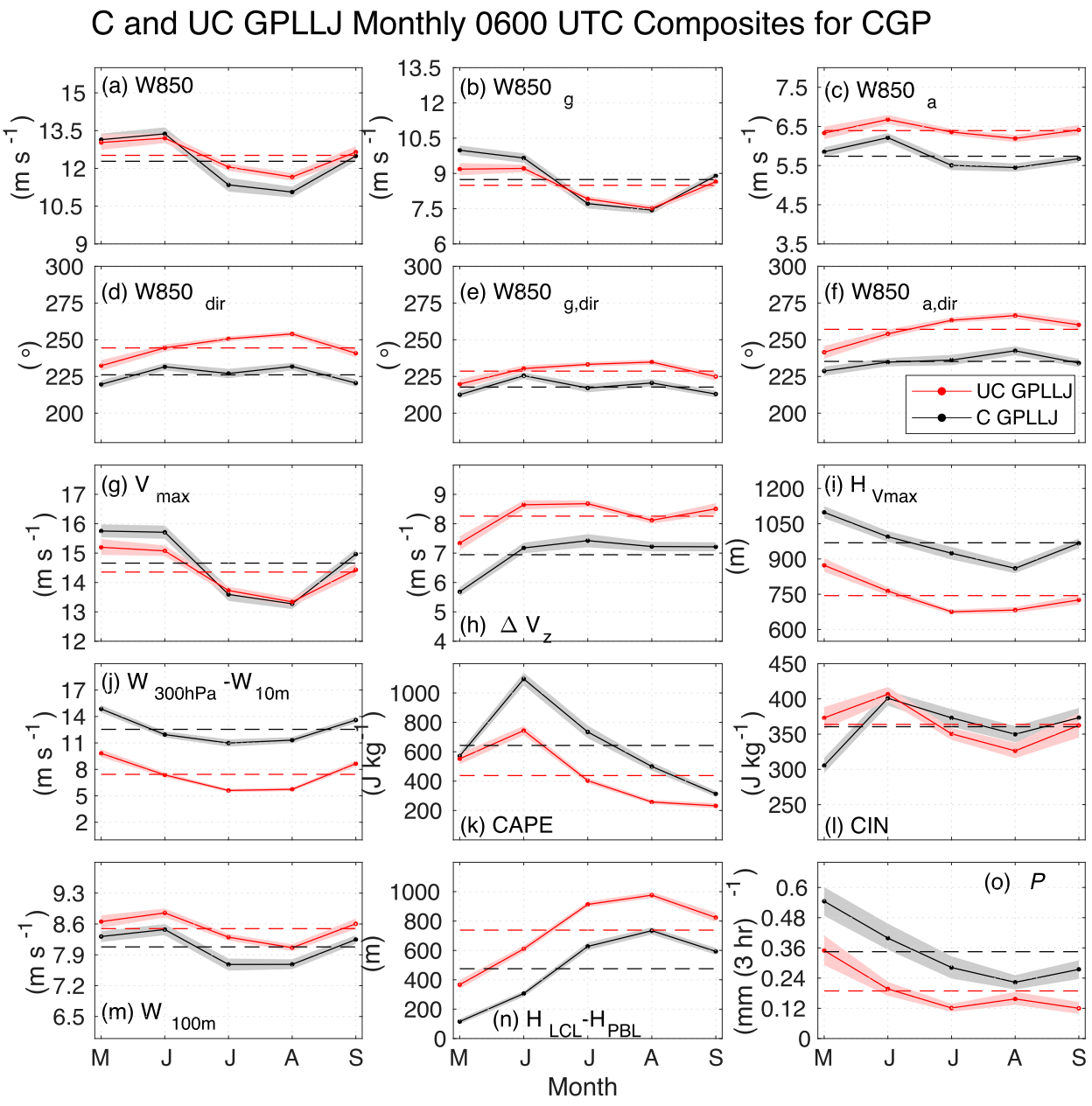

FIG. 11. As in Fig. 5, but for monthly 0600 UTC composites. Dashed lines represent the corresponding jet class sample MJJAS mean values. Corresponding sample size information is provided in Table 1. Note that *P* is accumulated from 0300 to 0600 UTC; all other fields are instantaneous. Summary statistics are provided in Table 2.

and monthly time scales because these are the time scales at which GPLLJ variability impacts severe weather potential (e.g., Campbell et al. 2019) and critical managed systems such as agriculture, commercial waterways, and an electric grid that depends on wind and hydropower generation.

This work focuses on the comparative analysis of representative, quasi-end-member C and UC GPLLJ samples for the southern-, central-, and northern Great Plains (SGP, CGP, and NGP, respectively) drawn from the 110-yr (1901–2010) 1.125° × 1.125° CERA-20C jet classification dataset of Burrows et al. (2019b). The specific variables of analysis include low-level wind parameters, Bonner–Whiteman GPLLJ criteria, precipitation, and parameters of atmospheric stability. An analysis of the daily and monthly time mean values of these fields, as well as their diurnal amplitude and seasonality reveals significant differences between C and UC GPLLJs both within a given subregion and across the latitudinal range spanned by the SGP, CGP, and NGP subregions.

The results show that C GPLLJs occur most frequently in the CGP during May and September, when the midlatitude jet

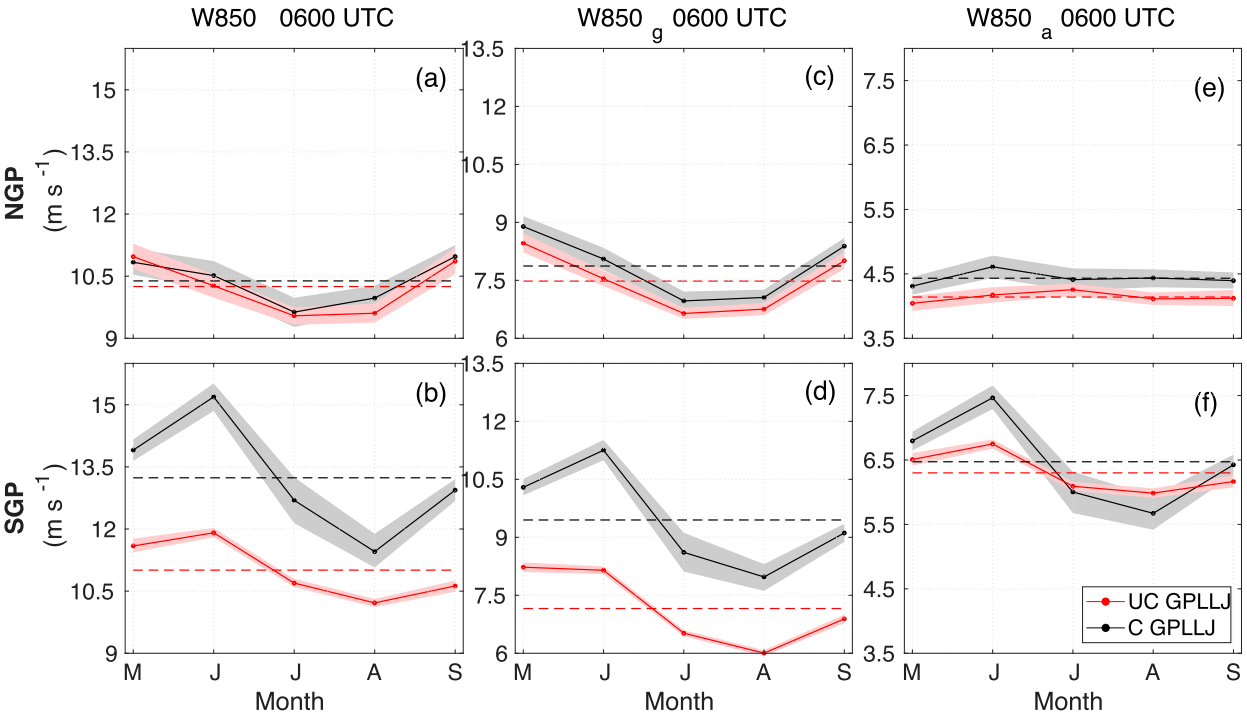

FIG. 12. 0600 UTC monthly composites of (a),(b) 850-hPa wind speed (W850), (c),(d) geostrophic W850 ($W850_g$), and (e),(f) ageostrophic W850 ($W850_a$) constructed from this study's filtered C (black) and UC (red) GPLLJ samples for the (a),(c),(e) NGP and (b),(d),(f) SGP. Line width indicates the 95% bootstrapped confidence interval for each monthly composite value.

stream is positioned more southerly and regional soil moisture is above MJJAS average (Figs. 2, 5). Relative to UC GPLLJs, C GPLLJs are characterized by similar near-surface wind magnitudes (except for SGP) but faster and more southerly jet winds ($V_{\max}$) at an $H_{V\max}$ that is on average 193 m higher than that of UC GPLLJ $H_{V\max}$, across all subregions at 0600 UTC. C GPLLJ jet noses tend to be broader and extend deeper into the atmosphere (Fig. 3) with greater 300-hPa–10 m vertical wind shear. Relatedly, it is possible that particularly deep C GPLLJ jets are being undersampled because they fail to meet the minimum Bonner–Whiteman $H_{V\max}$–700-hPa vertical wind shear (ΔV_z) threshold of 6 m s^{-1} (section 2b). The MJJAS-mean UC GPLLJ ΔV_z exceeds that of C GPLLJs by 1.0, 1.4, and 0.5 m s^{-1} for the NGP, CGP, and SGP, respectively. Overall, C GPLLJs are associated with more unstable atmospheric conditions than UC GPLLJs. Averaged over all subregions and months, C GPLLJs have 3.4 m s^{-1} greater 300-hPa–10-m wind shear, 137.6 J kg^{-1} more CAPE, and 0.13 mm (3 h)$^{-1}$ more P at 0600 UTC (Fig. 11).

Consistent with earlier literature (e.g., Mitchell et al. 1995; Wu and Raman 1998) and our expectation, most parameter fields were found to exhibit greater diurnal variability during UC GPLLJs compared to C GPLLJs (Figs. 5–10). This finding is expected because UC GPLLJs have a greater land–atmosphere forcing component and as such, should be more sensitive to the diurnal radiative cycle. As an example, C GPLLJ $V_{\max}$ exceeds 10 m s^{-1} at all times of day in all subregions considered, whereas UC GPLLJ $V_{\max}$ falls well below 10 m s^{-1} during daytime hours in the CGP and SGP. For simplicity and brevity, we presented only 0600 UTC monthly mean results. In future work, differentiation between jets could be optimized by using different variables at different times. Indeed, for some fields such as H_{LCL} (2100 UTC when PBL maximizes; Fig. S4) and P (0000 UTC when P maximizes; Figs. 5, 10) the time of maximum jet class differences does not correspond with 0600 UTC. Moreover, the optimal times for differentiation by parameter may also vary by region (e.g., SGP vs NGP). Due to limited sample sizes, we were not able to investigate monthly changes in diurnal variability, although we expect diurnal variability to peak in midsummer (i.e., June–July).

An important conclusion of this study is that while the magnitude of variables still differs significantly between jet types in all subregions, the diurnal variability of both jet classes similarly increases from north to south, reflecting greater land–atmosphere coupling for both jet classes in the SGP. We hypothesize this is attributable to 1) stronger geostrophic winds ($W850_g$) related to larger diurnal temperature ranges in the south's more arid climate and relatedly, a stronger Rockies–GP temperature gradient (i.e., Holton mechanism), combined with 2) greater ageostrophic winds ($W850_a$) and veering thereof after collapse of a relatively deeper PBL over dry soils (i.e., enhanced Blackadar inertial oscillation; Figs. 6, 7, S4, and S9). C and UC GPLLJs in the SGP, as well as UC GPLLJs in the CGP, exhibit distinct peaks in $W850_g$ around sunset (~0000 UTC) as expected by theory (Parish and Oolman 2010) that is not evident in the NGP results (Figs. 5, 6). Overall, the combined effect of greater Holton- and Blackadar-related diurnal forcing outsizes any effects of diminished Coriolis force in the SGP.

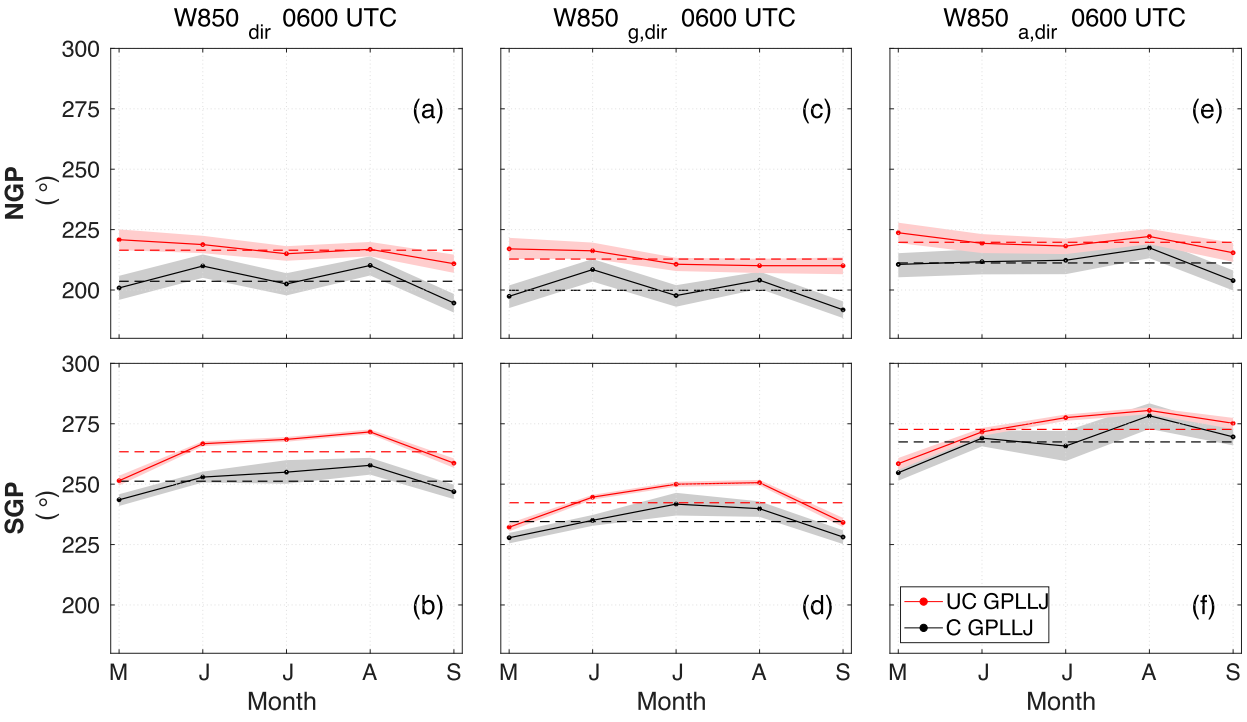

FIG. 13. As in Fig. 12, but for (a),(b) W850 direction ($W850_{dir}$), (c),(d) $W850_g$ direction ($W850_{g,dir}$), and (e),(f) $W850_a$ direction ($W850_{a,dir}$).

In general terms, the W850 and V_{max} winds, together with the diurnal amplitude of $W850_a$ rotation, may be used to quantify the relative contributions of Holton- and Blackadar-type mechanistic forcing. Relatedly, the most effective fields for distinguishing between C and UC GPLLJs at diurnal and monthly time scales are $W850_g$, V_{max}, H_{Vmax}, 300-hPa–10-m bulk shear, CAPE, and P (C GPLLJs will have larger magnitudes) and ΔV_z and CIN (UC GPLLJs will have larger magnitudes). Given a long enough dynamically classified jet record, a subset of these variables could potentially be used to artificially extend the classification record. Note that as with diurnal variability, the seasonality of all variables considered (e.g., Fig. 12) increases from north to south, as measured by the standard deviation of monthly mean values (Table 2).

Overall, this study underscores the importance of differentiating (and not conflating) C and UC GPLLJs in seasonal forecasts and climate projections (e.g., CMIP) because the two jet classes affect Great Plains hydroclimate, severe weather, and wind energy potential very differently. Studies that use V850 as a surrogate for GPLLJ strength and frequency (e.g., Tang et al. 2017; Harding and Snyder 2015; Weaver and Nigam 2008; Danco and Martin 2018; Malloy and Kirtman 2020) should be interpreted with caution not only due to the varied impacts of the respective jet classes, but because UC GPLLJs have a strong westerly wind component and are likely being undercounted. Future investigations into interannual to decadal variability of GPLLJ frequencies related to large-scale patterns, like the North Atlantic subtropical high (NASH; e.g., Li et al. 2012; He et al. 2017), ENSO, PDO, and the Pacific–North American (PNA) teleconnection pattern, should account for these different GPLLJ classes. This will facilitate better mechanistic understanding of the role of teleconnections in this region.

Finally, it is important to emphasize that this study contrasted strongly coupled and weakly coupled GPLLJ conditional samples that were explicitly constructed to highlight jet class differences. In the real world, the full range of upper-level GPLLJ coupling is represented; all GPLLJs have some degree of both land and atmospheric coupling. Thus, there is also further work to be done to quantify the degree of upper-level coupling on a continuous scale.

Acknowledgments. This work was funded by NSF Award AGS-1638936. DB performed all analyses. DB and CF cowrote the manuscript. All authors discussed the interpretation and presentation of results. CERA-20C data were obtained from ECMWF via a dedicated data portal (http://apps.ecmwf.int/datasets). NCAR's Research Data Archive, which hosts the Great Plains Low-Level Jet Occurrence and Upper-Level Coupling—CERA-20C dataset corresponding to this manuscript is sponsored by NSF.

REFERENCES

Arritt, R. W., T. D. Rink, M. Segal, D. P. Todey, C. A. Clark, M. J. Mitchell, and K. M. Labas, 1997: The Great Plains low-level jet during the warm season of 1993. *Mon. Wea. Rev.*, **125**, 2176–2192, https://doi.org/10.1175/1520-0493(1997)125<2176:TGPLLJ>2.0.CO;2.

Barandiaran, D., S. Y. Wang, and K. Hilburn, 2013: Observed trends in the Great Plains low-level jet and associated precipitation changes in relation to recent droughts. *Geophys. Res. Lett.*, **40**, 6247–6251, https://doi.org/10.1002/2013GL058296.

Berg, L. K., L. D. Riihimaki, Y. Qian, H. Yan, and M. Huang, 2015: The low-level jet over the southern Great Plains determined from observations and reanalyses and its impact on moisture transport. *J. Climate*, **28**, 6682–6706, https://doi.org/10.1175/JCLI-D-14-00719.1.

Blackadar, A. K., 1957: Boundary layer wind maxima and their significance for the growth of nocturnal inversions. *Bull. Amer. Meteor. Soc.*, **38**, 283–290, https://doi.org/10.1175/1520-0477-38.5.283.

Bonner, W. D., 1968: Climatology of the low level jet. *Mon. Wea. Rev.*, **96**, 833–850, https://doi.org/10.1175/1520-0493(1968)096<0833:COTLLJ>2.0.CO;2.

Burrows, D. A., C. R. Ferguson, M. A. Campbell, G. Xia, and L. F. Bosart, 2019a: An objective classification and analysis of upper-level coupling to the Great Plains low-level jet over the twentieth century. *J. Climate*, **32**, 7127–7152, https://doi.org/10.1175/JCLI-D-18-0891.1.

——, ——, and L. F. Bosart, 2019b: Great Plains low-level jet occurrence and upper-level coupling in CERA-20C. Research Data Archive at the National Center for Atmospheric Research, Computational and Information Systems Laboratory, accessed 28 January 2020, https://doi.org/10.5065/KDB5-9X72.

Campbell, M. A., C. R. Ferguson, D. A. Burrows, M. Beauharnois, G. Xia, and L. F. Bosart, 2019: Diurnal effects of regional soil moisture anomalies on the Great Plains low-level jet. *Mon. Wea. Rev.*, **147**, 4611–4631, https://doi.org/10.1175/MWR-D-19-0135.1.

Chen, G., J. Lu, D. A. Burrows, and R. L. Leung, 2015: Local finite-amplitude wave activity as an objective diagnostic of midlatitude extreme weather. *Geophys. Res. Lett.*, **42**, 10 952–10 960, https://doi.org/10.1002/2015GL066959.

Cook, K. H., E. K. Vizy, Z. S. Launer, and C. M. Patricola, 2008: Springtime intensification of the Great Plains low-level jet and Midwest precipitation in GCM Simulations of the twenty-first century. *J. Climate*, **21**, 6321–6340, https://doi.org/10.1175/2008JCLI2355.1.

Danco, J. F., and E. R. Martin, 2018: Understanding the influence of ENSO on the Great Plains low-level jet in CMIP5 models. *Climate Dyn.*, **51**, 1537–1558, https://doi.org/10.1007/s00382-017-3970-9.

Ferguson, C. R., E. F. Wood, and R. K. Vinukollu, 2012: A global intercomparison of modeled and observed land–atmosphere coupling. *J. Hydrometeor.*, **13**, 749–784, https://doi.org/10.1175/JHM-D-11-0119.1.

——, M. Pan, and T. Oki, 2018: The effect of global warming on future water availability: CMIP5 synthesis. *Water Resour. Res.*, **54**, 7791–7819, https://doi.org/10.1029/2018wr022792.

Frye, J. D., and T. L. Mote, 2010: The synergistic relationship between soil moisture and the low-level jet and its role on the prestorm environment in the southern Great Plains. *J. Appl. Meteor. Climatol.*, **49**, 775–791, https://doi.org/10.1175/2009JAMC2146.1.

Gelaro, R., and Coauthors, 2017: The Modern-Era Retrospective Analysis for Research and Applications, version 2 (MERRA-2). *J. Climate*, **30**, 5419–5454, https://doi.org/10.1175/JCLI-D-16-0758.1.

Harding, K. J., and P. K. Snyder, 2015: The relationship between the Pacific–North American teleconnection pattern, the Great Plains low-level jet, and north central U.S. heavy rainfall events. *J. Climate*, **28**, 6729–6742, https://doi.org/10.1175/JCLI-D-14-00657.1.

He, C., B. Wu, L. Zou, and T. Zhou, 2017: Responses of the summertime subtropical anticyclones to global warming. *J. Climate*, **30**, 6465–6479, https://doi.org/10.1175/JCLI-D-16-0529.1.

Helfand, H. M., and S. D. Schubert, 1995: Climatology of the simulated Great Plains low-level jet and its contribution to the continental moisture budget of the United States. *J. Climate*, **8**, 784–806, https://doi.org/10.1175/1520-0442(1995)008<0784:COTSGP>2.0.CO;2.

Hersbach, H., and Coauthors, 2020: The ERA5 global reanalysis. *Quart. J. Roy. Meteor. Soc.*, **146**, 1999–2049, https://doi.org/10.1002/qj.3803.

Higgins, R. W., Y. Yao, E. S. Yarosh, J. E. Janowiak, and K. C. Mo, 1997: Influence of the Great Plains low-level jet on summertime precipitation and moisture transport over the central United States. *J. Climate*, **10**, 481–507, https://doi.org/10.1175/1520-0442(1997)010<0481:IOTGPL>2.0.CO;2.

Hodges, D., and Z. Pu, 2018: Correction to: Characteristics and variations of low-level jets in the contrasting warm season precipitation extremes of 2006 and 2007 over the southern Great Plains. *Theor. Appl. Climatol.*, **136**, 773–774, https://doi.org/10.1007/s00704-018-2492-7.

——, and ——, 2019: Characteristics and variations of low-level jets and environmental factors associated with summer precipitation extremes over the Great Plains. *J. Climate*, **32**, 5123–5144, https://doi.org/10.1175/JCLI-D-18-0553.1.

Holton, J. R., 1967: The diurnal boundary layer wind oscillation above sloping terrain. *Tellus*, **19**, 200–205, https://doi.org/10.3402/tellusa.v19i2.9766.

Huang, C. S.-Y., and N. Nakamura, 2016: Local finite-amplitude wave activity as a diagnostic of anomalous weather events. *J. Atmos. Sci.*, **73**, 211–229, https://doi.org/10.1175/JAS-D-15-0194.1.

Jiang, X., N.-C. Lau, I. M. Held, and J. J. Ploshay, 2007: Mechanisms of the Great Plains low-level jet as simulated in an AGCM. *J. Atmos. Sci.*, **64**, 532–547, https://doi.org/10.1175/JAS3847.1.

Laloyaux, P., E. De Boisséson, and P. Dahlgren, 2017: CERA-20C: An Earth system approach to climate reanalysis. *ECMWF Newsletter*, No. 150, ECMWF, Reading, United Kingdom, 25–30, https://www.ecmwf.int/en/elibrary/18164-cera-20c-earth-system-approach-climate-reanalysis.

——, and Coauthors, 2018: CERA-20C: A coupled reanalysis of the twentieth century. *J. Adv. Model. Earth Syst.*, **10**, 1172–1195, https://doi.org/10.1029/2018MS001273.

Li, L., W. Li, and Y. Kushnir, 2012: Variation of the North Atlantic subtropical high western ridge and its implication to southeastern US summer precipitation. *Climate Dyn.*, **39**, 1401–1412, https://doi.org/10.1007/s00382-011-1214-y.

Maddox, R. A., 1983: Large-scale meteorological conditions associated with midlatitude, mesoscale convective complexes. *Mon. Wea. Rev.*, **111**, 1475–1493, https://doi.org/10.1175/1520-0493(1983)111<1475:LSMCAW>2.0.CO;2.

Malloy, K. M., and B. P. Kirtman, 2020: Predictability of midsummer Great Plains low-level jet and associated precipitation. *Wea. Forecasting*, **35**, 215–235, https://doi.org/10.1175/WAF-D-19-0103.1.

Martineau, P., G. Chen, and D. A. Burrows, 2017: Wave events: Climatology, trends, and relationship to Northern Hemisphere winter blocking and weather extremes. *J. Climate*, **30**, 5675–5697, https://doi.org/10.1175/JCLI-D-16-0692.1.

Mitchell, M. J., R. W. Arritt, and K. Labas, 1995: A climatology of the warm season Great Plains low-level jet using wind profiler observations. *Wea. Forecasting*, **10**, 576–591, https://doi.org/10.1175/1520-0434(1995)010<0576:ACOTWS>2.0.CO;2.

Newton, C. W., 1967: Severe convective storms. *Advances in Geophysics*, Vol. 12, Academic Press, 257–308, https://doi.org/10.1016/S0065-2687(08)60377-5.

Nikolic, J., S. Zhong, L. Pei, X. Bian, W. E. Heilman, and J. J. Charney, 2019: Sensitivity of low-level jets to land-use and land-cover change over the continental U.S. *Atmosphere*, **10**, 174, https://doi.org/10.3390/atmos10040174.

Parish, T. R., 2017: On the forcing of the summertime Great Plains low-level jet. *J. Atmos. Sci.*, **74**, 3937–3953, https://doi.org/10.1175/JAS-D-17-0059.1.

——, and L. D. Oolman, 2010: On the role of sloping terrain in the forcing of the Great Plains low-level jet. *J. Atmos. Sci.*, **67**, 2690–2699, https://doi.org/10.1175/2010JAS3368.1.

Reif, D. W., and H. B. Bluestein, 2017: A 20-year climatology of nocturnal convection initiation over the central and southern Great Plains during the warm season. *Mon. Wea. Rev.*, **145**, 1615–1639, https://doi.org/10.1175/MWR-D-16-0340.1.

Santanello, J. A., C. D. Peters-Lidard, and S. V. Kumar, 2011: Diagnosing the sensitivity of local land–atmosphere coupling via the soil moisture–boundary layer interaction. *J. Hydrometeor.*, **12**, 766–786, https://doi.org/10.1175/JHM-D-10-05014.1.

Shapiro, A., and E. Fedorovich, 2010: Analytical description of a nocturnal low-level jet. *Quart. J. Roy. Meteor. Soc.*, **136**, 1255–1262, https://doi.org/10.1002/qj.628.

——, ——, and S. Rahimi, 2016: A unified theory for the Great Plains nocturnal low-level jet. *J. Atmos. Sci.*, **73**, 3037–3057, https://doi.org/10.1175/JAS-D-15-0307.1.

Song, F., Z. Feng, R. L. Leung, R. A. Houze Jr., J. Wang, J. Hardin, and C. R. Homeyer, 2019: Contrasting spring and summer large-scale environments associated with mesoscale convective systems over the U.S. Great Plains. *J. Climate*, **32**, 6749–6767, https://doi.org/10.1175/JCLI-D-18-0839.1.

Squitieri, B. J., and W. A. Gallus, 2016a: WRF forecasts of Great Plains nocturnal low-level jet-driven MCSs. Part I: Correlation between low-level jet forecast accuracy and MCS precipitation forecast skill. *Wea. Forecasting*, **31**, 1301–1323, https://doi.org/10.1175/WAF-D-15-0151.1.

——, and ——, 2016b: WRF forecasts of Great Plains nocturnal low-level jet-driven MCSs. Part II: Differences between strongly and weakly forced low-level jet environments. *Wea. Forecasting*, **31**, 1491–1510, https://doi.org/10.1175/WAF-D-15-0150.1.

Tang, Y., J. A. Winkler, S. Zhong, X. Bian, D. L. Doubler, L. Yu, and C. K. Walters, 2017: Future changes in the climatology of the Great Plains low-level jet derived from fine resolution multi-model simulations. *Sci. Rep.*, **7**, 5029, https://doi.org/10.1038/s41598-017-05135-0.

Tuttle, J. D., and C. A. Davis, 2013: Modulation of the diurnal cycle of warm-season precipitation by short-wave troughs. *J. Atmos. Sci.*, **70**, 1710–1726, https://doi.org/10.1175/JAS-D-12-0181.1.

Uccellini, L. W., 1980: On the role of upper tropospheric jet streaks and leeside cyclogenesis in the development of low-level jets in the Great Plains. *Mon. Wea. Rev.*, **108**, 1689–1696, https://doi.org/10.1175/1520-0493(1980)108<1689:OTROUT>2.0.CO;2.

Walters, C. K., 2001: Airflow configurations of warm season southerly low-level wind maxima in the Great Plains. Part II: The synoptic and subsynoptic-scale environment. *Wea. Forecasting*, **16**, 531–551, https://doi.org/10.1175/1520-0434(2001)016<0531:ACOWSS>2.0.CO;2.

——, and J. A. Winkler, 2001: Airflow configurations of warm season southerly low-level wind maxima in the Great Plains. Part I: Spatial and temporal characteristics and relationship to convection. *Wea. Forecasting*, **16**, 513–530, https://doi.org/10.1175/1520-0434(2001)016<0531:ACOWSS>2.0.CO;2.

Wang, S. Y., and T.-C. Chen, 2009: The late-spring maximum of rainfall over the U.S. central plains and the role of the low-level jet. *J. Climate*, **22**, 4696–4709, https://doi.org/10.1175/2009JCLI2719.1.

——, X. A. Chen, and J. Correia, 2011: Climatology of summer midtropospheric perturbations in the U.S. northern plains. Part I: Influence on northwest flow severe weather outbreaks. *Climate Dyn.*, **36**, 793–810, https://doi.org/10.1007/s00382-009-0696-3.

Weaver, S. J., and S. Nigam, 2008: Variability of the Great Plains low-level jet: Large-scale circulation context and hydroclimate impacts. *J. Climate*, **21**, 1532–1551, https://doi.org/10.1175/2007JCLI1586.1.

——, S. D. Schubert, and H. Wang, 2009: Warm season variations in the low-level circulation and precipitation over the central United States in observations, AMIP simulations, and Idealized SST experiments. *J. Climate*, **22**, 5401–5420, https://doi.org/10.1175/2009JCLI2984.1.

——, S. Baxter, and A. Kumar, 2012: Climatic role of North American low-level jets on U.S. regional tornado activity. *J. Climate*, **25**, 6666–6683, https://doi.org/10.1175/JCLI-D-11-00568.1.

Weng, S.-P., 2000: A new perspective on the regional hydrologic cycle over North and South America. Ph.D. thesis, Iowa State University, 153 pp.

Whiteman, C. D., X. Bian, and S. Zhong, 1997: Low-level jet climatology from enhanced rawinsonde observations at a site in the southern Great Plains. *J. Appl. Meteor.*, **36**, 1363–1376, https://doi.org/10.1175/1520-0450(1997)036<1363:LLJCFE>2.0.CO;2.

Wiser, R., and M. Bolinger, 2019: 2018 wind technologies market report. Office of Energy Efficiency and Renewable Energy, U.S. Department of Energy, 103 pp., https://www.energy.gov/sites/prod/files/2019/08/f65/2018%20Wind%20Technologies%20Market%20Report%20FINAL.pdf.

Wu, Y., and S. Raman, 1998: The summertime Great Plains low level jet and the effect of its origin on moisture transport. *Bound.-Layer Meteor.*, **88**, 445–466, https://doi.org/10.1023/A:1001518302649.

Yang, S., X. Ding, D. Zheng, and Q. Li, 2007: Depiction of the variations of Great Plains precipitation and its relationship with tropical central-eastern pacific SST. *J. Appl. Meteor. Climatol.*, **46**, 136–153, https://doi.org/10.1175/JAM2455.1.